Department of Chemistry

University College London

# Investigating the low hydrothermal stability of Cu/SAPO-34 in $NH_3$-SCR

## A computational and experimental approach

Daniel Silva Nunes


Submitted in partial fulfilment of the requirements for the degree of Masters in Research (MRes) at University College London on the26th of August 2016

# Acknowledgments

I would like to thank Professor Ian Robinson, Professor Richard Catlow and Dr Scott Woodely for the interesting and helpful discussions thorough the process of this investigation.

I would also like to thank Dr Rachel O'Malley for her support and fruitful discussions during our beamtimes at I-13.

Special thanks to my mum and grandparents for all the emotional support and wise words.

Finally, I would like to thank the $M^3S$ programme for providing me with the opportunity to learn about a field that I love.

# *Abstract*

A lot interest has been paid in the use of Cu/SAPO-34 for $NH_3$-SCR, the reduction of $NO_x$ in the present of ammonia. However, there have reports that, in spite of being very good at converting NO*x* into $N_2$ and $H_2O$, less hazardous gases to the atmosphere, Cu/SAPO-34 has poor hydrothermal stability at relatively low temperature. One of the arguments is that this catalytic deactivation is achieved as a result of a re-arrangement of the Cu sites in the zeolite into an inactive form.

In the light of this information, this study aimed to find out what effect the presence of water has on structure distorting phenomena, such as NTE or the development of strain in the crystal structure in the present of water. The former case aimed to be tackled via molecular modelling methodologies, whereas the latter using an imaging technique called BCDI.

The molecular modelling work successfully predicated RUMs mediated NTE behaviour in AlPO-34, H/SAPO-34 and Cu/SAPO-34. PXRD results yielded the same results but with slightly different lattice parameters values. BCDI revealed that high humidity levels increase the Cu/SAPO-34 is found to be more strained than at less humid conditions.

# Table of Contents

# *List of Figures*

# *Chapter I*

# *Research Motivation*

The historical intensification of greenhouse gas emissions to the atmosphere has led to an increase in the average temperature of the Earth; a phenomenon known as global warming.[1] Greenhouse gases such as hydrocarbons (HC), carbon monoxide (CO) or nitrous oxides ($NO_x$), are known to be emitted by stationary and mobile power stations.[2] Although there are many examples that fit any one of these two categories, this work will focus on one particular example of a mobile power station: in general terms the automotive engine, namely the automotive exhaust emission control associated with it. This emission control has been the focus of research that aims to perfect its efficiency, due to the ever more restrictive policies legislated to prevent hazardous amounts of greenhouse gases from being emitted to the atmosphere.[1,3]

A successful example of such an exhaust emission control technology is the three-way catalytic converter (TWC), normally found in gasoline powered vehicles.[4] A general illustration of a TWC is seen in ***Figure 1a***. This system is so-called 'three-way' because is able to perform three of operations more or less simultaneously: the reduction of $NO_x$ into nitrogen ($N_2$) and oxygen ($O_2$) gases; the oxidation of CO to carbon dioxide ($CO_2$) and the oxidation of HC to $CO_2$ and water ($H_2O$). The catalysis of such reactions is normally performed by a family of microporous materials known as zeolites, demonstrated in ***Figure 1a*** by the yellow honeycomb-like structure.[5] Although such TWCs do well in the 'rich burn' regime, wherein the combustion process takes place at an almost stoichiometric air/fuel ratio (AFR), the automotive industry has been keen to move towards TWCs that operate under "lean burn" regime instead; wherein there is a high AFR and thus less fuel is required for the combustion process. However, as depicted by the graph in ***Figure 1b***, the conversion efficiency of $NO_x$ drastically falls under this "lean burn" regime for higher AFR, whereas for the other two gases it remains constant. The last decade has been marked by significant interest into tackling this 'lean-$NO_x$' emission control problem.

Johnson Matthey (JM) has been interested in the use of copper-exchanged silicoaluminophosphate-34 (Cu/SAPO-34) for the reduction of $NO_x$ by using ammonia ($NH_3$) - a process known as selective reduction catalysis (SCR), $NH_3$-SCR. Cu/SAPO-34 shows high efficiency at high AFR, and as a result JM has issued a patent to protect their intellectual know-how for the use of Cu/SAPO-34 in $NH_3$-SCR .[6] However, in spite of its high efficiency in converting $NO_x$, Cu/SAPO-34 has been recently reported to have low hydrostability at relatively low temperatures.[7] This instability at these conditions is alarming because they are the sort of conditions found during engine start-ups. The authors of this study suggested that

this catalytic deactivation might arise because geometric the re-arrangement of the Cu sites into an inactive form.[7]

In the light of this suggestion and of the enthusiasm that JM has to ensure that its products are world class efficient, the current work aims to establish some grounding in the science of this problem in two ways: (*i*) by using molecular modelling techniques to determine whether Cu/SAPO-34 displays negative thermal expansion (NTE)[8] behaviour and, if so, whether such behaviour is impacted by the presence of $H_2O$ molecules and (*ii*) a Bragg coherent diffraction imaging (BCDI)[9] investigation on the development of strain in Cu/SAPO-34 crystals to establish if strain develops differently at different locations in these crystals in the presence of $H_2O$.

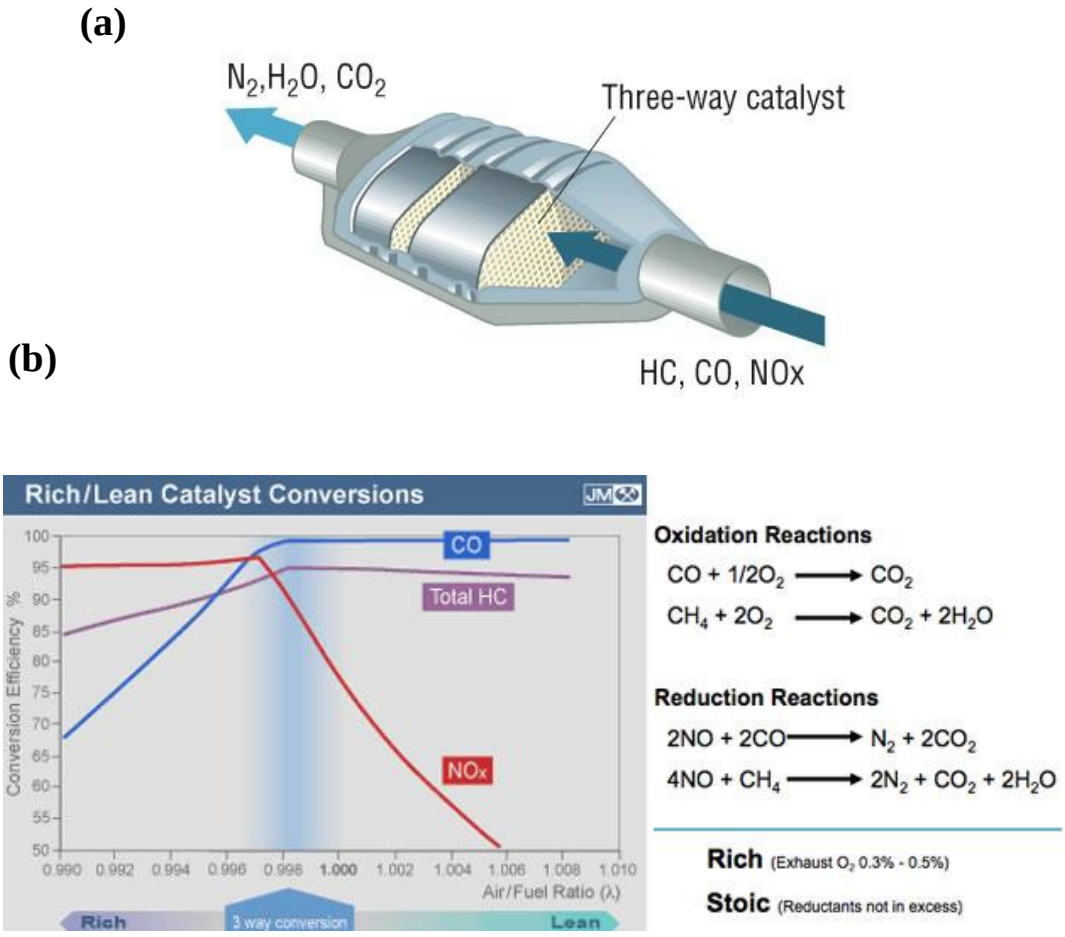


***Figure 1***. ***(a)*** An illustration of a three-way catalyst found in catalytic converters. ***(b)*** The catalytic efficiency of the conversion of hydrocarbons (HC), carbon monoxide (CO) and nitrous oxides ($NO_x$).[10]

# *Chapter II*

# *Introduction*

## 2.1. A general introduction on zeolites

### 2.1.1. General structure

Zeolites are crystalline microporous materials which structure and properties allow for a number of useful applications that have been exploited by both the chemical industries and academia.[11] These materials are normally used as catalysts, for the purpose of molecular sieving and in ion-exchange processes.[11,12] The zeolite structure normally consists of silicon cations ($Si^{4+}$) and aluminum cations ($Al^{3+}$) which are surrounded by four oxygen anions ($O^{2}$); whereby each $O^{2-}$ connects the $Si^{4+}$ and $Al^{3+}$ to each other. This results in a macromolecular three-dimensional framework made up of $SiO_2$ (neutral) and $AlO_2^-$ (negatively charged) tetrahedral building blocks. The overall negatively charged structure is neutralized by the presence of extra-framework cations such as hydrogen ($H^+$) that bond to the $O^{2-}$ throughout the zeolite structure. This leads to the formation of OH Brønsted acid sites that are highly active in catalysis. An illustration of a general zeolite structure is seen on ***Figure 2.***

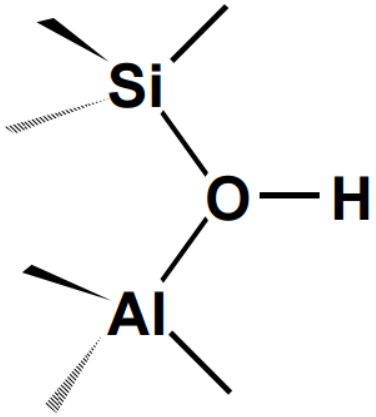


***Figure 2.*** A general depiction of the two tetrahedral building blocks, $SiO_2$ and $AlO_2^-$, and a OH Brønsted acid site.

The arrangement of these tetrahedral building blocks gives rise to a pore system with channels in one, two or three dimensions. Depending on the topology of the structure, the pore size may range from 3 Å to 12 Å. The size of these pores, and thus the topology of the zeolites, is paramount to determine what sort of application the zeolites can be used for. Consider the example of molecular sieving: the size of the pores will be intimately linked

with the size of the molecules that one wants to filter out of a solution; water purification is a classic illustration of this.

### 2.1.2. SAPOs and AlPOs

Although zeolites are mostly made of $SiO_2$ and $AlO_2^-$ tetrahedral building blocks, there are systems that also contain $PO_2^+$ tetrahedral building blocks in their framework; the relative elemental distribution of Si, Al, and P arises via a series of substitution reactions during the synthesis of the material. The proposed mechanisms for these substitution reactions are discussed in ***section 2*** of this chapter. As a result of the charge disparity, given that $SiO_2$ is neutral and $PO_2^+$ is positively charged, there will often less extra-framework ions to neutralise the system as more substitutions are the proportion of $PO_2^+$ to $SiO_2$ increases. When system only contains $PO_2^+$ and $AlO_2^-$, the system is classified as an aluminophosphate (AlPO), which is charge neutral. In spite one finding zeolites, SAPOs, and AlPOs are are isostructural to each other (SAPO-34 is a good example of this, as it will be discussed later on), these will display different degrees of Brønsted acidity. This leads to different electronic properties and thus different catalytic properties too.

## 2.2. The structure SAPO-34

As it was elaborated in ***Chapter I***, Cu/SAPO-34 has been found to be a good catalyst for the purpose of $NH_3$-SCR. This section will concentrate on introducing the reader to the structure of SAPO-34 and extra pieces of information that will be useful to put into context the investigation that is discussed in this work.

### 2.2.1. Structure and Si insertion mechanisms

SAPO-34 is a small pore zeolite based on the *Chabasite* (CHA) structure. The CHA structure is characterized by a barrel-shaped cage made up of double six member rings (*D6R*s) – two connected rings of six tetrahedral $Si^{4+}/Al^{3+}/P^{5+}$ ions linked by $O^{2-}$. Once these rings are arranged an identical layer fashion (AAA…), and subsequently stacked, the structure is yielded. The topology of the CHA structure generates three different sized member rings (MR): four member rings (4MR), six member rings (6MR) and eight member rings (8MR),

as seen in ***Figure 3***. The pore size of SAPO-34 is normally of the order of 3.8 Å (a good size for the diffusion of the reactant and product molecules involved in $NH_3$-SCR). This topology allows for four different Brønsted acid sites; which correspond to four distinct oxygen atoms. SAPO-34 is isostructural to two other systems: SSZ-13 and AlPO-34. The difference between these three materials lies on the relative amounts of $SiO_2$ to $PO_2^+$; whereby SSZ-13 has no $PO_2^+$ and AlPO-34 no $SiO_2$.

Martens *et al.*,[13] has proposed two different substitution mechanisms for Si insertion, each one of them leading to different consequences when it comes to the Si distribution in the SAPO structure. Although the chemical mechanisms themselves are still being investigated, the mechanism's reaction equations have been widely accepted; these are illustrated here by the formation of H/SAPO-34 from AlPO-34. The first mechanism, denoted substitution mechanism two (SM2) is given by ***equation 1***. In this case, a $P^{5+}$ is substituted for a $Si^{4+}$ and an extra-framework ion, $H^+$. Substituting in this manner, generally leads to a distribution of *isolated* Si, whereby each $Si^{4+}$ has at least three ions ($Al^{3+}$ and $P^{5+}$) between each other. The second possible substitution mechanism is known as SM2+SM3, as seen in ***equation 2***. In this case both $P^{5+}$ and $Al^{3+}$ are substituted for $Si^{4+}$ ions and extra-framework ions, $H^+$. The SM3 mechanism starts via SM2 to substitute a $P^{5+}$ and then an $Al^{3+}$. In contrast to purely SM2, this mechanism leads to the generation of agglomerates of $Si^{4+}$. These agglomerates are formally known as Si *islands*. In spite of generating initially only an *isolated* Si configuration, if the SM2 mechanism is repeated over a number of times, depending on the topology of the structure, there will be no way to avoid the formation of Si *islands*. Each structural topology has a threshold value beyond which the Si *island* configuration becomes dominant over the *isolated* Si one.

$$\textbf{SM2:}\ [AlPO_4] + 3Si^{4+} + 3H^+ \longrightarrow [3Si,3H]_P + 3P^{5+} \qquad \textit{(1)}$$

$$\textbf{SM2 + SM3:}\ [AlPO_4] + 5Si^{4+} + 3H^+ \longrightarrow [5Si,3H]_{Al,P} + 4P^{5+} + Al^{3+} \qquad \textit{(2)}$$

For the CHA structure topology, this threshold value is approximately 10%; as derived by Barthomeuf.[14] This threshold value holds independently of extra-framework ion. It is important to stress the fact that it is still possible to find Si *islands* under this threshold value, it is just less likely than finding the *isolated* Si distribution.

The relative extent of Si incorporation via these two mechanisms may be computed from the framework composition (*i.e.* via the Si molar fraction) of the SAPO-34 structure.[15]

The relative amount of Si incorporated via the SM2 mechanism is seen in ***equation 3*** and that for SM3 in ***equation 4***; where *x* denotes the molar fraction of a given element.

$$x_{Si}\,(SM2) = x_{Al} - x_{P} \quad \textbf{(3)}$$

$$x_{Si}\,(SM3) = 1 - 2x_{Al} \quad \textbf{(4)}$$

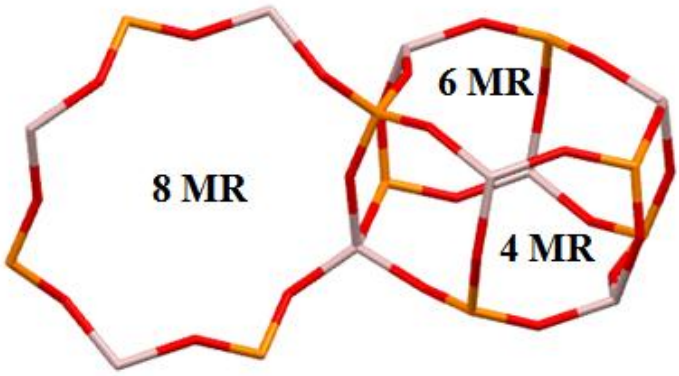


***Figure 3.*** An illustration of the CHA structure. Three types of MRs are found in the structure a result of the stacking pattern of the barrel shaped cage made up of double six member rings. In this case, the red vertices denote $O^{2-}$ anions, the orange vertices are $P^{5+}$ cations and the grey vertices illustrate the $Al^{3+}$ cations.

### 2.2.2. The position of Cu in Cu/SAPO-34

The position of the Cu sites in SAPO-34, namely for the purposes of $NH_3$-SCR is a still discussed in the literature. However it has been proposed that the following are the most probable sites to find the Cu ions coordinated to the SAPO-34 framework, as illustrated by ***Figure 4***:[16] (I) the Cu ion is found displaced from the 6 MR into the ellipsoidal cavity; (II) the Cu ion is located near the centre of this ellipsoidal cavity; (III) the Cu is found in the hexagonal prism and (IV) the Cu ion is located near the 8MR window. In the context of the $NH_3$-SCR, sites (I) and (IV) seem to be most interesting.[16]

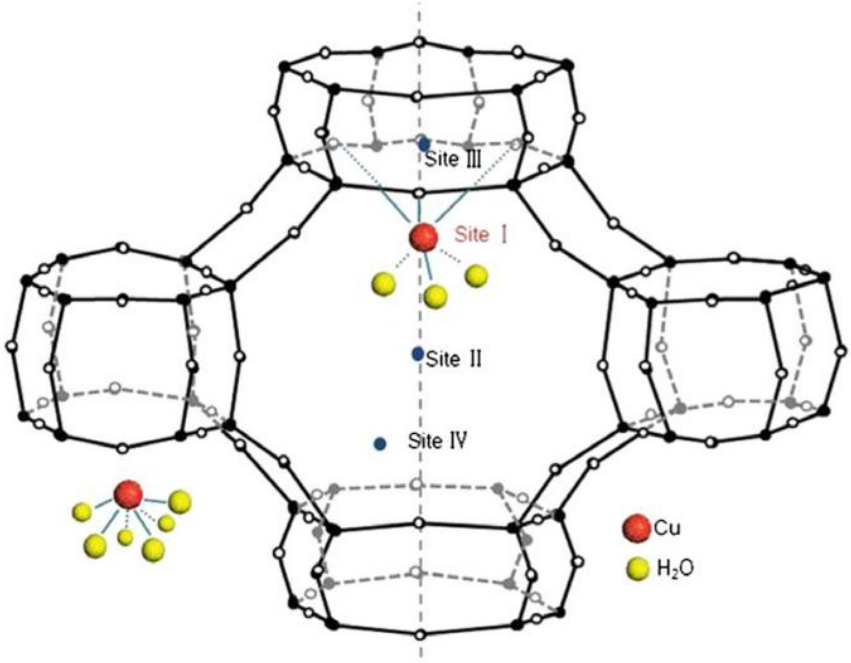


***Figure 4.*** A schematic of the unit cell of SAPO-34. In this case, the solid circle illustrates an $Al^{3+}$, $P^{5+}$ and $Si^{4+}$ and the open circles represent the oxygens.[16]

### 2.2.3. Deactivation of Cu/SAPO-34 in $NH_3$-SCR

As it was highlighted in ***Chapter I***, although Cu/SAPO-34 shows good rate of conversion of $NO_x$, there it has been reported that, at certain conditions, the system becomes deactivated. Leistner *et al.* concluded that there was a $NO_x$ conversion decrease from 87% to 66% at 200 $^oC$, after leaving Cu/SAPO-34 for three hours at 70 $^oC$.[7] The team argues that this loss of effectiveness is down to a transformation of the active Cu sites into an inactive form. The team also reported that the deactivation was not reversed upon attempting to regenerate the catalyst. More recently, Arstad *et al.* attempted to investigate the possible deactivation of SAPO-34, not for the purpose of $NH_3$-SCR, but for the Methanol to Olefins (MTO) process; widely use in petrochemical industry.[17] The team found that the decrease in performance of SAPO-34 in this case was due to a redistribution of Si. They argue that the redistribution led to the formation of Si *islands* with a concomitant loss of Brønsted acid sties and thus reducing the catalytic activity. Although Arstad does not discuss the possible consequence that this might have for the case of Cu/SAPO-34 in the $NH_3$-SCR, it could be that the formation of Si *islands* in this Cu/SAPO-34 may distort the framework to the point of yielding the inactive form of the active Cu site proposed by Leistner.

### 2.2.4. Other relevant structural information

#### 2.2.4.1. The diffractogram of SAPO-34

The structure of SAPO-34 has been extensively studied in the literature via x-ray diffraction. An example of a diffractogram of Cu/SAPO-34 produced by Martínez-Franco *et al*. is illustration ***Figure 6***.[18] The SAPO-34 framework is known to have rhombohedral symmetry, belonging to the $R\bar{3}m$ space group.

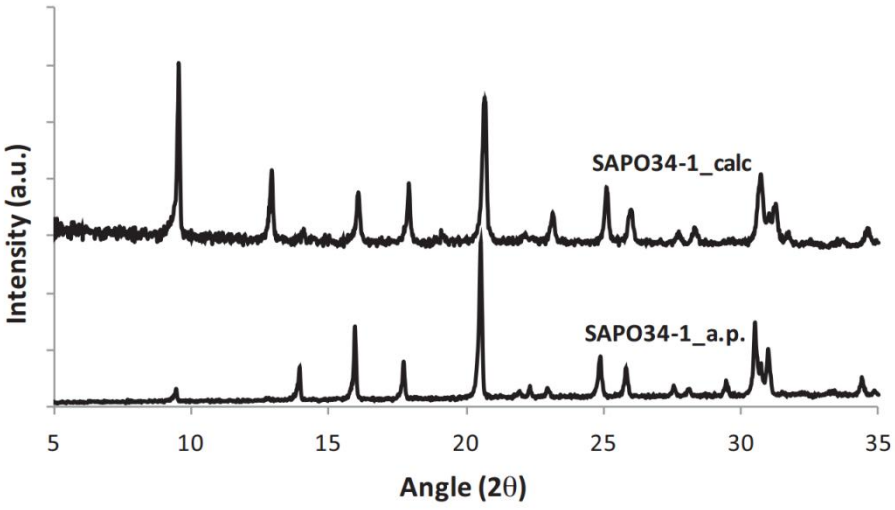


***Figure 5.*** The XRD patterns of Cu/SAPO-34 in its calcined and *as-prepared* forms, as published by Martínez-Franco *et al*.[18]

#### 2.2.4.2. SAPO-34 crystal morphology

As it was concluded by Iwase *et al,* the crystals of SAPO-34 appear to have an approximate regular, cubic shape.[19] This morphology seems to be independent of the extra-framework ion, since publications showing the crystal morphology of various 'versions' of SAPO-34 all seem to come to the same conclusion. An illustration of the crystal morphology of SAPO-34 obtained via scanning electron microscopy by Iwase *et al*. is seen in ***Figure 6.***[19]

### 2.2.4.3. The possibility of stacking faults

Although the structure of SAPO-34 is thought to be quite crystalline, the possibility of one finding stacking faults in the framework has been reported in the literature.[20] The authors of this study state these faults are yield as a result of displacement stacking faults during the synthesis process. Displacement stacking faults occur when the sequence AAA… (which is the case for the CHA framework) is disturbed by a dislocation of the layers or via the occurrence of a different layer type. Sławinski *et al*. argue that in this case of SAPO-34 this fault originates through the insertion of an additional B type layer into the AAA… starting layer sequence. Thus AAA… becomes ABA…, as illustrated in ***Figure 7***. It will become apparent later in the subsequent work that, although SAPO-34 crystals are accepted as being quite crystalline, this might not be the case (see ***Chapter V***).

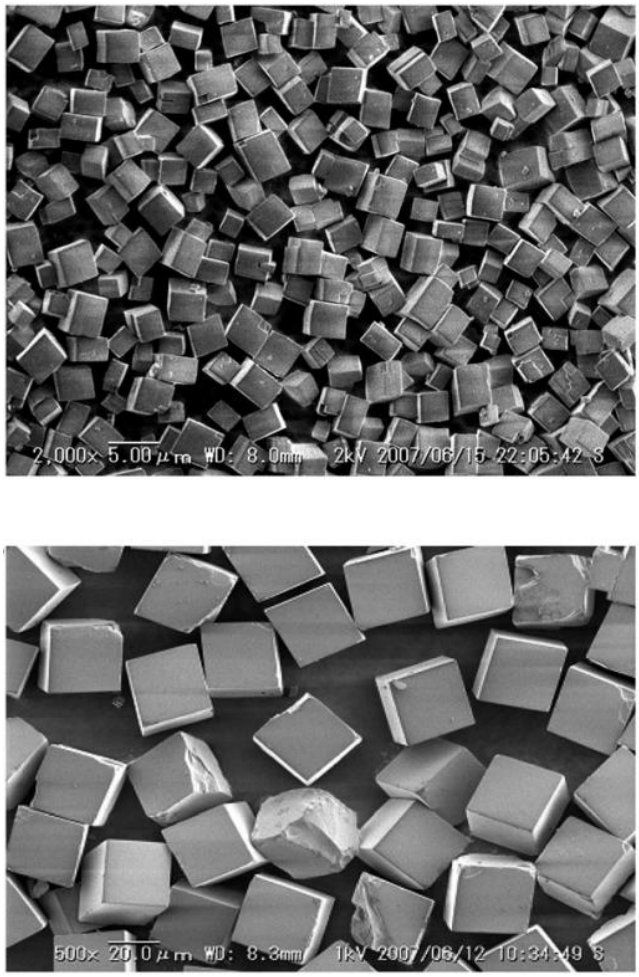


***Figure 6.*** An example of SEM images of SAPO-34, as obtained by Iwase *et al*.[19]

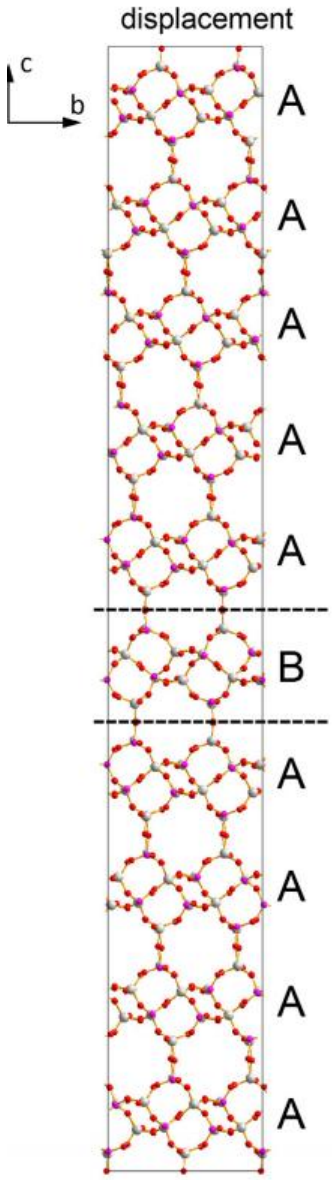


***Figure 7.*** A depiction of the stacking fault, originated by way of insertion of a different layer, postulated by Sławiński *et al*.[20]

The remaining portion of this chapter aims to introduce the reader to the concept of NTE and the different mechanisms via which the this phenomenon may arise in solid state systems, such as zeolites.

## 2.3. Thermal Expansion

If one heats up a solid, it would be expected, mundanely, for its volume to increase, this phenomenon is known as positive thermal expansion (PTE). The mechanism by which PTE arises can be explained by using a two-body potential; a trace that describes how the energy of a system varies as a function of the separation between two bodies (***Figure 8***). In the case of two atoms, let their interatomic distance be *r*. In ***Figure 8***, the equilibrium position (minimum of the function) is found at *r* = 3. Near to the minimum point, the function's form can be described via a quadratic expression**,** and thus it would be expected for it to be symmetric on either side of *r* = 3. This approximation is called Hooke's law (or the harmonic spring model).[21] It is clear however that, as *r* tends to either zero or infinity, this approximation breaks down because, under these limits, the function is not symmetric anymore. This lack of symmetry occurs because the vibrations between the two atoms are actually anharmonic (*i.e.* not harmonic) in nature. In the anharmonic model, as *r* tends to zero, the energy increases much faster than in the quadratic case, a consequence of the Pauli Exclusion Principle.[22] When *r* tends to infinity the energy also increases but only up to a certain value of *r*. The gradient of the curve becomes increasingly closer to zero as *r* approaches infinity; above a certain interatomic distance the bonding becomes negligible and its energy is hence zero (*i.e.* bond dissociation takes place). This asymmetry on either side of the equilibrium distance causes an excursion to longer interatomic distances and thus the average interatomic distance will increase with increasing energy. The analytical expression for the anharmonic function is seen in ***equation 5***, where $E_v$ represents the energy of the system at the $v^{th}$ vibrational level, *v* is the vibrational quantum number, and $x_e$ and $y_e$ correspond to the first and second anharmonicity constants.

$$\boldsymbol{E_v = \left(v + \frac{1}{2}\right) v_e - \left(v + \frac{1}{2}\right)^2 v_e x_e + \left(v + \frac{1}{2}\right)^3 v_e y_e + \ higher\ terms} \quad \textbf{(5)}$$

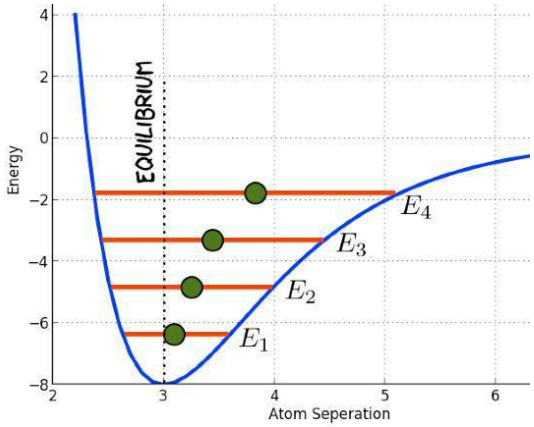


***Figure 8.*** An illustration of a interatomic potential energy curve. As the energy increases the particle, depicted by the green circle tends to found at longer interatomic distances at each energy level ($E_1$, $E_2$, *etc*). This is a result of the asymmetry of the function.[23]

The extent of thermal expansion is captured by the thermal expansion coefficient, α. There are two ways of expressing α; either with regards of how the volume of the solid changes with temperature, $\alpha_V$ (***equation 6***), or to how the length of the material changes with temperature, $\alpha_l$ (***equation 7***), where *dV* and *dl* represent the changes in volume and length, respectively, $V_0$ and $l_0$ denote the volume and length prior to expansion/contraction and *dT* is the change in temperature.

$$\boldsymbol{\alpha_V = \frac{dV}{V_0 dT}} \quad \textit{(6)}$$

$$\boldsymbol{\alpha_l = \frac{dl}{l_0 dT}} \quad \textit{(7)}$$

A useful relationship for the case of isotropic materials (those which expand at equal rate in all three directions) is the one in ***equation 8***. For anisotropic solids (those which expand at different rates in one, two or three directions) this relationship is not as straightforward and thus one may have to compute the individual contribution of the three crystallographic axes - *a*, *b* and *c* - towards $\alpha_V$ (***equation 9***).

$$\boldsymbol{\alpha_V = 3\alpha_l} \quad \textit{(8)}$$

$$\boldsymbol{\alpha_V = \alpha_a + \alpha_b + \alpha_c} \quad \textit{(9)}$$

Another important concept when discussing thermal expansion is the Grüneisen parameter, γ. This parameter describes how the Debye temperature, θ (*i.e.* the temperature of a crystal's highest normal mode of vibration), depends on the volume, ***equation 10***. The Grüneisen parameter is also related to by ***equation 11***; $C_D$ denotes the Debye specific illustrated heat capacity and K is the bulk modulus. Since γ and K are weakly dependent on temperature,$\alpha_l$ will show a temperature dependency very close to that of $C_D$; the latter is in expressed in ***equation 12***.

$$\boldsymbol{\gamma = -\frac{\partial ln\theta}{\partial V}} \qquad \textbf{(10)}$$

$$\boldsymbol{\alpha_l = \frac{\gamma C_D}{3KV}} \qquad \textbf{(11)}$$

By using the concepts covered so far, the way how the volume varies in the temperature can be derived (***equation 13***). When γ and K are known, ***equation 13*** is normally used to fit experimental thermal expansion by refining θ - for the ease of the analysis functions are used to approximate the integration in this equation.

$$\boldsymbol{C_D = 9Nk_B\left(\frac{T}{\theta}\right)^3 \int_0^{\frac{\theta}{T}} \frac{x^4 e^x}{(e^x-1)^2}} \qquad \textbf{(12)}$$

$$\boldsymbol{V(T) = V_0 + \frac{9Nk_B}{K}\left(\frac{T}{\theta}\right)^3 \int_0^{\frac{\theta}{T}} \frac{x^3}{e^x-1}} \qquad \textbf{(13)}$$

It is also possible to conclude from the expression of ***equation 13*** that the volume is proportional to the temperature. This is in agreement with the interpretations made from the interatomic potential of ***Figure 8***.

However, there are materials that contract upon heating. At first glance it could be said that these materials do not follow the theory discussed thus far. Consequently, the aim of the next section is to review the proposed mechanisms by which this phenomenon arises.

## 2.4. Negative Thermal Expansion

Some solids contract upon heating. Such materials are known as NTE materials. Examples of these solids are found in a variety of different material families such as metal oxides,[24,25] zeolites,[26,27] AlPOs[28,29] or metal-organic frameworks.[30,31] This inverse proportionality between the volume and the temperature is reflected by a negative Grüneisen parameter, γ. Because of the dependency between and γ (***equation 10***), $\alpha_l$, and consequently negative $\alpha_V$ (***equation 7***), will be negative. The reader should be aware that the values of α that are normally published on scientific journals are normally an average $\alpha_V$, with respect to the $\alpha_l$ of each crystallographic axis. As discussed by Sleight, some materials might expand in one direction and contract in the other two or vice versa; these materials are said to expand anisotropically.[32] Throughout the years a number of mechanisms to explain the NTE phenomenon in solids have been proposed. These mechanisms can be separated into two categories. One is the category of mechanisms that occur as a result of the properties of the material, which is called intrinsic NTE and a second that is based on the mechanisms that promote NTE behaviour via external sources, known as extrinsic NTE. The aim of the rest of this chapter is to discuss all these mechanisms.

### 2.4.1 Intrinsic NTE Mechanisms

Within this category one finds three families of mechanisms *(i)* framework; *(ii)* atomic radius contraction, *(iii)* magnetovolume and *(iv)* phase transition.

#### 2.4.1.1. Framework

In his famous publication, Sleight suggested four different ways in which NTE could occur within framework materials.[33] These four mechanisms are mostly seen in metal oxides.[24,31,34]

(1) Increased regularity in polyhedra: The average metal-oxygen (M-O) bond distances found in the polyhedra of metal oxides tends to decrease as the polyhedra become more regular.[35] In some $AMO_3$ oxides with the perovskite structure, this increased regularity is developed by an increase in the temperature.[36] Sleight argued that the contraction of the M-O bond distance can be attributed to the reduced anion-anion repulsions, promoted by the increased polyhedral regularity. Thus increased temperatures will lead to smaller volumes. Two examples of such oxides are $BaTiO_3$ and $PbTiO_3$.[36] This effect has been found to be oddly strong in $PbTiO_3$

because both $PbO_{12}$ and $TiO_6$ polyhedra change significantly within the tetragonal phase of the material. In both $BaTiO_3$ and $PbTiO_3$ the NTE is anisotropic; expansion along the *a* and *b* axes and contraction along the *c* axis.[32] Once these materials transit to their cubic phase (higher degree of symmetry) at higher temperatures this effect disappears and positive thermal expansion is found in all three crystallographic axes. No examples of oxides displaying an isotropic NTE behaviour via this mechanism have been found in the literature. However, it shouldn't be impossible to find materials where this mechanism is found within the cubic phase.[37]

(2) Expansion/contraction response: In some cases, a material may positively expand in one direction and negatively expand in the other two, or vice versa (anisotropic NTE).[32] Examples of two oxides that show highly anisotropic NTE are NZP, $NaZr_2P_3O_{12}$, (which contracts along the *a* and *b* axes, and expands along the *c* axis), and *β*-eucryptite, $LiAlSiO_4$, (which expand along the *a* and *b* axes, and contracts along the c axis). In the case of NZP, Sleight suggested that its anisotropy arises because the chains of the face shared octahedra present in its structure expand, along the *c* axis, upon heating. This expansion ultimately pulls the chains together along the *a* and *b* axes by virtue of the twist of the phosphorous-oxygen (P-O) bonds. With regards to β-eucryptite, an increase in the temperature leads to an expansion of the sheets of edge sharing polyhedra in its structure and a pulling along the *c* axis, as illustrated in ***Figure 9***.

(3) Interstitial cation re-distribution mechanism: This mechanism is mostly important in materials with a significant ionic conductivity. In the case of *β*-eucryptite, the $Li^+$ cations move from their 'native' tetrahedral sites to others of octahedral geometry.[33] Upon modeling this system, it was suggested that the movement of the $Li^+$ ions as a function of the temperature lead to NTE behaviour in the material.[33] Although a slightly different system-type, it would be interesting to investigate how the re-distribution of extra-framework ions, normally found in systems that require their addition to achieve increased activity, such as in the case of Cu/SAPO-34, changes the NTE behaviour of the solid (assuming NTE behaviour is present to start with!) - no such studies have been found in the literature during the conception of this work.

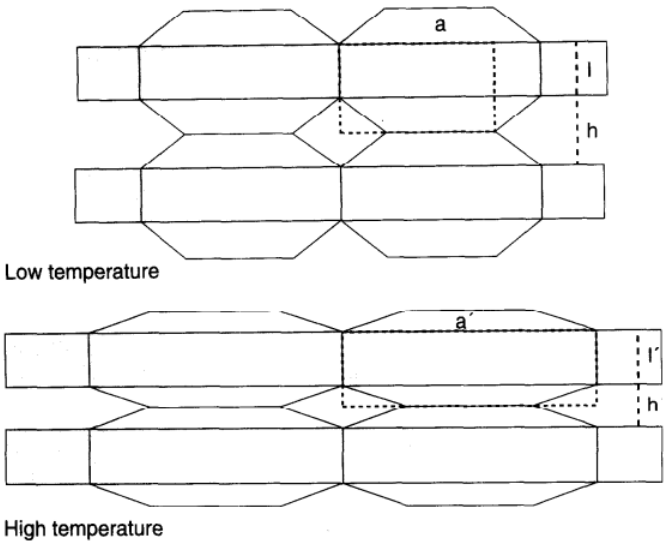


***Figure 9.*** This pictures illustrates the effect of anisotropic thermal expansion (a mixture of positive and negative thermal expansion) in two dimensions. As the temperature increases the length along a increases and the length along h decreases.[32]

(4) Rigid unit model mechanism: Out of all four mechanisms here discussed, this is perhaps the most widely used to explain the NTE behaviour of polyhedra-based solids. NTE materials within this category are characterised by strong bonds. Referring back to the interatomic potential curve of ***Figure 8***, systems with stronger bonds are characterised by more symmetric (thus more harmonic) and narrower wells. As it was explained previously, harmonic potential wells should give rise to no expansion, since the potential does not have the characteristics ascertained in ***section 3***. When it comes to thermal expansion, there are two key phonon modes; longitudinal and transverse phonon vibrations. As illustrated in ***Figure 10a***, longitudinal modes increase the metal-oxygen (M-O) bond distances within the solid upon heating - applicable to 'positive' thermal expansion. In the case of the transverse modes (***Figure 10b***) the increased temperature leads a decrease of the metal-metal distances (M---M) because of the increased amplitude of the M-O-M bond angle. Transverse vibrational modes are less energetic than longitudinal modes and thus can be excited at lower temperatures. Since both vibrational modes occur somewhat simultaneously, their effect on the M---M distance will depend on which one is dominant. For the case of phonons, the relationship between the Grüneisen parameter, $\gamma$, and a given phonon mode is shown in ***equation 14***, where $\omega$ is the frequency of the vibrational mode and *s* is the applied strain. By

looking at relationship between ***equation 11*** and ***14***, it can be determined that a volume contraction is associated with a decrease of ω. In the case of systems where transverse phonon modes are dominant, one should expect the near-zero ω to be highly populated relatively to the higher ω.[34]

$$\gamma = -\frac{1}{2\omega^2}\frac{\delta\omega^2}{\delta s} \quad (14)$$

Examples of materials that display such characteristics are $ZrW_2O_8$ (which adopts the perovskite structure), some zeolites.[34,38–40] Such materials have $MO_4$ units (where M is a metal cation), illustrated in ***Figure 11a***. In such scenario, the M-O-M linkages behave like hinges. Importantly, the $MO_4$ unit is much stiffer when compared to the M-O-M linkage because the former has much higher frequency phonon modes - known as rigid unit modes (RUMs).[41,42] When temperature is increased, it is far more favourable to rotate or to bend the M-O-M hinges than it is to distort the stiff $MO_4$ unit. Such rotation and bending (***Figure 11***) lead to a reduction of the structure's volume. This model was developed by Hammond et al. in the late nineties.[41] It is important to mention that these 'hinges' are not necessarily just M-O-M. Below room temperature, copper oxide ($Cu_2O$) contracts upon heating because of the reduced O-Cu-O bond angle and not due to the Cu-O-Cu one.

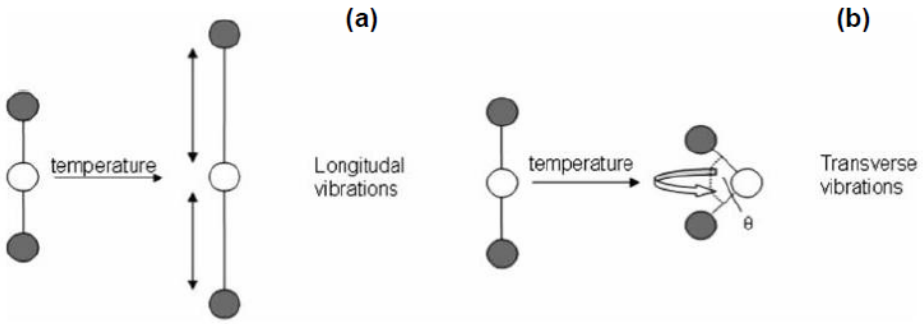


***Figure 10.*** The two important phonon modes in thermal expansion; (a) the longitudinal phonon mode and (b) the transverse phonon mode.[43]

In contrast to RUMs, quasi RUMs (QRUMs) have low frequency and not 'near-zero' frequency and thus are higher in energy. Consequently, either some or all the rigid polyhedra are capable of rotation and distortion. This was shown to be true for $ZrV_2O_7$ by Pryde *et al*.[44] In this system, the rotation of the $VO_4$ tetrahedrons causes significant distortions to the $ZrO_6$ octahedrons. The preference towards the distortion of the M-O-M linkages is explained by the strong repulsions between the O atoms. The rotation of the hinges has anharmonic character and its vibration can be expressed via the Grüneisen parameter of ***equation 14***.

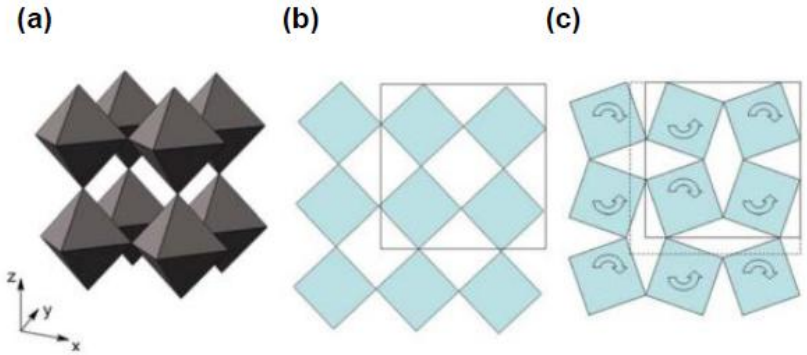


***Figure 11.*** An illustration of the reduction in volume of the perovskite structure, (a), as a result of the RUMs. If one depicts ***(a)*** in 2D it leads to ***(b)*** where the square represent the space filed by the four blue diamonds in ***(b)***. Increasing the temperature leads to a tilting of the diamonds (which corresponds to a rotation of the tetrahedra). This rotation ultimately leads to a reduction of the volume depicted but the decrease of the area of the square in the ***(c)***.[43]

### 2.4.1.2. Atomic radius contraction

Unlike the previous mechanism, where the NTE behaviour was related to structure, systems within this category contract upon heating due to variation in the atomic (ionic) radii by way of charge transfer – the atom accepting electrons will expand whereas the one donating them will contract. $Sm_{2.75}C_{60}$, as reported by Arvantidis et al., is an example of this case.[45] Within this model, volume contraction occurs when the expansion of the acceptor atom is smaller than the contraction of the donator atom. Importantly, among other factors, the atomic radius depends on the spin configuration of the atom.[46] Generally, an atom in its high-spin state has a larger radius than when its low-spin state – the Pauli Exclusion Principle demands that, in the high-spin case, electrons must populate different orbitals.[22] Recently this effect has been

found to take place in perovskite materials.[47–50]

### 2.4.1.3. Magnetovolume effect

It has been determined that some solids contract because of a variation in the amplitude of their magnetic moment as a consequence of a temperature increase. According to the electronic theory of solids, an increased volume hinders the overlap of the electronic orbitals in a system, which consequently leads to a narrowing of the bands in the solid's band structure. This band narrowing subsequently increases the density of states at the Fermi level and at this stage magnetism is preferred. This is called the magnetovolume effect. The first material shown to display such behaviour was Fe-36Ni Invar ($\alpha = 0.5 – 1$ ppm $K^{-1}$ below its Curie temperature of 500 K).[51,52] Its discoverer, Guillaume, was awarded the Nobel Prize for it in 1920.[51] Fe-36Ni Invar also displays the mechanism of atomic radius contraction: the increase in temperature leads to a transfer of the electron population from the high-spin state (large radius) in the Fe ions to the low-spin state (shorter radius). More recently it has been shown that this effect is also present in maganese nitrides.[52] In this investigation it was found that, for the system $Ag_{1-x}NMn_{3+x}$, composition variation has an effect on the NTE behaviour of this material. The Ag to Mn exchange leads to a broadening of the temperature range within which the magnetovolume effect can operate.

### 2.4.1.4. Phase transition

As previously discussed, RUMs occur in materials which structures have rigid polyhedra. However, it has been found that some solids that do exhibit NTE behaviour and rigid polyhedral do not rotate at all.[53] Thus their NTE properties cannot be explained via the RUMs mechanism. Phase transitions have been determined to be responsible to the rise of NTE behaviour in some solids.[53] Compounds of formula $A_2(MoO_4)_3$ and ferrierite (a zeolite) are two examples of such materials. Evans et al. investigated $Sc_2(MoO_4)_3$ and showed that its monoclinic had a positive $\alpha_V$ but its orthorhombic phase had a negative $\alpha_V$.[54] More recently it has been suggested that, since symmetry is of great importance to NTE, the change in the sign of $\alpha_V$ is promoted by the change of symmetry of the crystal by way of phase transition. More recently, Ardit and co-workers have proposed that the zeolite ZSM-5 may display this mechanism too.[55]

## 2.2.2. Extrinsic NTE Mechanisms

In addition to intrinsic NTE mechanisms there are others that are related to external sources. If existent, these operate along aside the intrinsic mechanisms.

(1) The presence of water: It has been suggested by Cruciani et al. that, although NTE behaviour of dehydrated analcime ($Na_{15.87}Al_{15.20}Si_{32.64}O_{96}$) had been explained by Hammonds and co-workers purely via the RUMs model,[41] the contraction of the natural zeolite was a result of framework relaxation due to complete dehydration. Cruciani argued that the diffusion of water molecules through the [111] channels in analcime during dehydration caused the six-ring apertures to open as widely as possible in order to facilitate water expulsion.[56] This distortion is followed by a relaxation process within which the T-O-T angle (where T denotes the tetragon in the structure) is restored to their initial values. As a consequence of the results obtained, the team suggested that the distortion and subsequent relaxation as a function of temperature are features of NTE behaviour. They also suggest that this contribution towards the NTE behaviour of analcime is complimented by RUMs.[41,42]

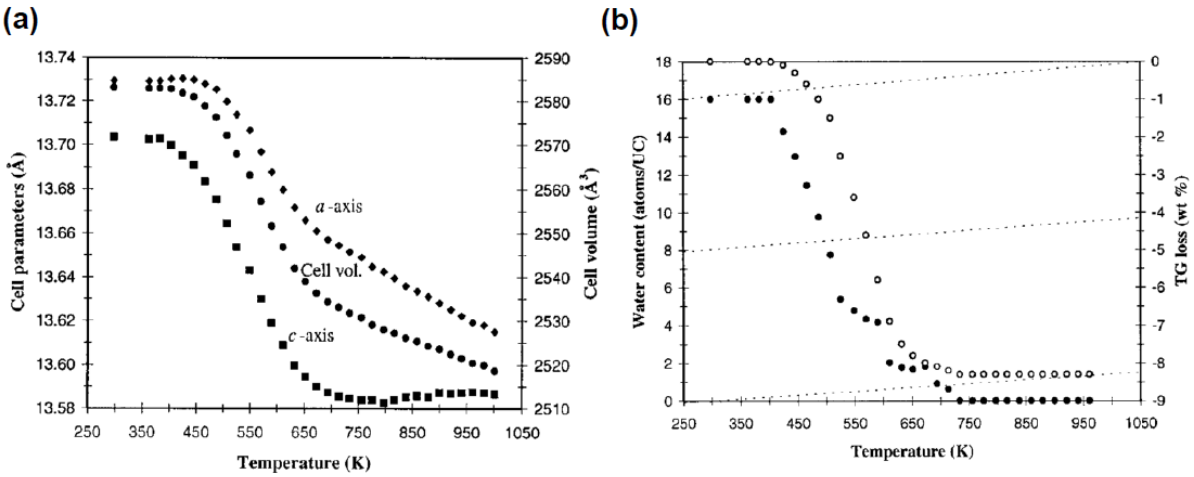


***Figure 12.*** The results obtained by Cruciani et al. whilst investigating the dehydration effects on the volume of analcime.[56] ***Figure 12(a)*** depicts the response of the crystallographic axis a (diamonds) and c (circles), and the cell volume (squares) to an increase in temperature. ***Figure 12(b)*** illustrates a comparison of the amount of water loss via refined occupancy (open circles; left axis) and via thermogravimetric (TG) loss (full circles; right axis) of analcime.

(2) Dealumination: In a study conducted Sen and co-workers to explore the effect of the concentration Al on the NTE behaviour of orthorhombic H[Al]ZSM-5 over a temperature range between 473 K and 1173 K.[26] The team found that the Al content had a profound effect on the NTE behaviour of the zeolites. Two different Al concentrations were studied; one with Si:Al ratio 250:1 and a second with Si:Al ratio of 27.5:1. Over this temperature range it was determined that the thermal expansion coefficient profile of these two zeolites changed drastically. The former exhibited a volume contraction over the entire temperature range for all three crystallographic axes. Its average expansion coefficient was found to be -34 x $10^{-6}$ $K^{-1}$. The authors argue that this is value is only surpassed by the anhydrous $AlPO_4$-17 discussed by Attfield and Sleight.[29] On the other hand the zeolite with a ratio of 27.5:1 showed a variation of its thermal expansion properties. Between 473 K and 673 K it expands positively whereas from 673K up to 1173K it expands negatively. To the team's knowledge, this was the first report of the effect of small changes in the Al concentration to the overall volume of ZSM-5. Furthermore, they reported the average positive expansion coefficient to be 39 x $10^{-6}$ $K^{-1}$ and the average negative expansion coefficient to be -85 $10^{-6}$ $K^{-1}$. More recently Marinkovic *et al.* studied the same system and proposed that the volume contraction that Sen and co-workers verified was not a consequence of dealumination but due to dehydration of the zeolite.[40] However this dispute is rather confusing since the experiment was performed at a temperature range between 350 $^{o}$C and 400 $^{o}$C, rather at the temperature range used by Sen and his co-workers. As it was discussed in the previous section, dehydration is known to contribute to NTE behaviour. No other examples of literature commenting on this type of effect were found in the literature. Thus further studies would be of great benefit to better understand the mechanisms and the function of the Al concentration with the NTE area.

# *Chapter III*

# *Methodological Concepts*

This chapter aims to elucidate the reader with some of the concepts that underpin each one of the techniques utilized throughout this investigation and that the reader may not be familiar with.

## 3.1. Interatomic Potentials

Molecules are formed by the interaction between atoms and ions. These interactions can be often characterised by their range, being short or long, or by their type, being covalent, ionic or metallic. In order to model the structure and properties of a molecular systems correctly, a more or less sophisticated mathematical construct that summarises all (or most) of the interactions within the molecule ought to be generated. The correlation between the interatomic (or interionic) distances and the interaction energy give rise to the so-called potential energy functions. The total energy of a system can be expressed as the sum of a number of terms that describe the difference types of interactions between the elements of a system, in this case atoms or ions. An example of such an expression is seen on ***equation 15***, where *U* denotes the total energy, *r* the interatomic distance, *V* is the energy of interaction, and *i*, and *j* and *k* correspond to the atoms or ions. Generally, an increased number of terms lead to a more accurate result, however this also leads to an increased computational cost.

The molecular modelling studies that were performed by using the General Utility Lattice Program (GULP) code.[57] Apart from the self-interaction term, first term in ***equation 15,*** three additional terms were used to compute the lattice energy for each molecular model: (*i*) Coulombic term, which describes the electrostatic interaction between the ions (long-range interaction), (*ii*) a Buckingham potential, which describes the short-range interactions between two bodies, expressed in ***equation 16***; *A* corresponds to size of the cation, ρ relates to the 'squishiness' of the anion and r denotes the interatomic distance between atoms *i* and *j*. The exponential term expresses the repulsive nature of the interactions at smaller interatomic distances than the equilibrium distance. The remainder factor represents the dispersion of the interaction at larger interatomic distances than the interatomic equilibrium distance. Finally, (*iii*) a three body that describes the bending of the bonds in the system.

$$\boldsymbol{U}(\boldsymbol{r}) = \sum_i \boldsymbol{V}_i(\boldsymbol{r}_i) + \frac{\mathbf{1}}{\mathbf{2!}} + \sum_{i<j} \boldsymbol{V}_{i,j}(\boldsymbol{r}_i, \boldsymbol{r}_j) + \frac{\mathbf{1}}{\mathbf{3!}} \sum_{i<j<k} \boldsymbol{V}_{ijk}(\boldsymbol{r}_i, \boldsymbol{r}_j, \boldsymbol{r}_k) + \cdots \qquad \textbf{(15)}$$

$$V(r) = A_{ij} e^{r_{ij}/\rho_{ij}} - \frac{C_{ij}}{r_{ij}^6} \qquad (16)$$

A caveat with regards to calculation of the long-range Coloumbic term, is the fact that, the system is periodic, there is no real way of telling where the system starts and ends, as expressed by the diverging series in ***equation 17***. Alas this summation may also be evaluated over delta (δ)-like charge densities eather than point charges themselves (***equation 18*****)** and ultimately expand these in a Fourier series. However, since a Fourier representation of a δ function requires an infinite amount of terms to be expressed, the Fourier space computation would still run into convergence problems. To overcome this problem, the Ewald summation method can be used. In this technique whereby the long-range interaction in the periodic system is divided into two well-behaved parts: (*i)* short-range contribution, which calculation is based on real space and (*ii*) a long-range contribution, which is computed in *k*-space by making use of Gaussian functions (***equation 19***). Upon computing the individual real space and *k*-space interactions, these can be summed in order to obtain the converged solution to the problem. An illustration of this last point is found in ***Figure 13.***

$$\varphi(r_i) = q \sum_{j+=1}^{\infty} \frac{1}{|r_i - r_{j+}|} - q \sum_{j-=1}^{\infty} \frac{1}{|r_i - r_{j-}|} \qquad (17)$$

$$\rho(r) = q \sum_{j+=1}^{\infty} \delta(r - r_{j+}) - q \sum_{j-=1}^{\infty} \delta(r - r_{j-}) \qquad (18)$$

$$\rho'(r) = -q_j \left(\frac{\eta}{\pi}\right)^{\frac{3}{2}} e^{-\eta^2 (r - r_j)^2} \qquad (19)$$

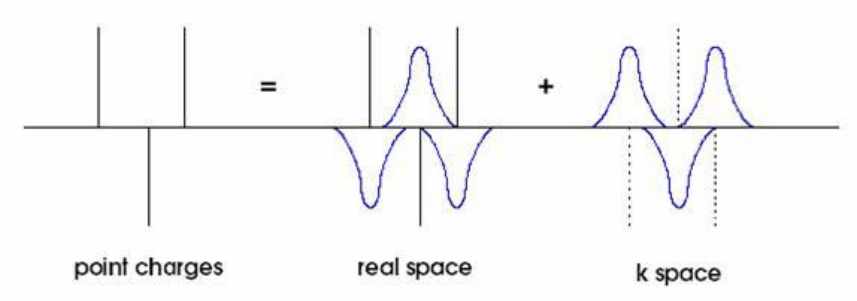


***Figure 13.*** An illustration of the Ewald summation.[58]

In addition to the interatomic potential, a core-shell model was also employed. This model is used to mimic the polarizability of the electron cloud on each atom/ion; this property may be computed by using ***equation 20***, where α is the polarizability, $q_s$ and $q_c$ the charge on the shell and core, respectively and *k* is the force constant of the harmonic spring. The overall picture of how the interactions between the ions were represented in the proceeding calculations can be seen in ***Figure 14***. If the atoms/ions are not polarizable they will only be described as a core and in a core/shell fashion if polarizable. In ***Figure 14*** a number of springs are portrayed: S1 is the spring that corresponds the interaction between the shells of the atoms, S2 is the spring that denotes the interaction between the cores of the atoms and S3 is used to mimic the polarizability of the atom. Naturally, each one of these springs will have an associated spring constant, *k*; which for S1 and S2 expresses the strength of the interaction and for S3 expresses how soft the atom is.

$$\alpha = \frac{2q_s^2 - q_c^2}{k} \qquad (20)$$

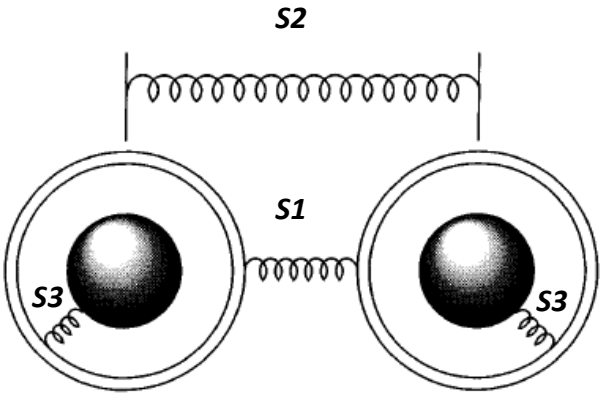


***Figure 14.*** An illustration of the core-shell model for a diatomic molecule.[59]

## 3.2. Energy optimisation techniques and the BFGS algorithm

Generally, once an appropriate interatomic potential has been selected, the next step is to ensure that all the properties that are to be computed for the chemical system correspond to its most preferred configuration. In more practically terms, it means that one has to ensure that the geometry of the molecule or of the unit cell of the crystal is the most preferred one. To achieve this geometry optimisation, numerical methods are used to scan the potential energy surface (PES), an *N*-dimensional description of the potential energy function; where *N* is the number of possible interactions within the system. By changing the coordinates of the atoms/ions, the PES can be explored until a point of relatively lower energy is found. These points can either be called a local minimum or a global minimum, where the latter is the lowest point energy in the entire PES. A general depiction of a PES is seen in ***Figure 15***. Various numerical methods have been developed to find these energy minima and, in the case of the current work, the Broyden-Fletcher-Goldfarb-Shannon (BFGS) algorithm was employed.

In a nutshell, the BFGS algorithm attempts to approximate the Hessian matrix of the PES. The Hessian is a symmetric second order matrix that describes the curvature of the PES. Consequently, in order to find a minimum, the algorithm aims to iteratively find a point in the landscape for which Hessian matrix elements are close to zero. A general representation of a *N*-dimensional Hessian matrix for a general function, *f*, is seen in ***equation 21***. To successfully reduce the matrix elements of the Hessian, the algorithm starts by generating a direction for the displacement of the initial position of the system in the PES to one where

some of the elements of the Hessians are lower than the current position. Upon displacing the system, the new Hessian for the new spatial point is approximated. This process is repeated iteratively until the Hessian matrix elements and the energy of the system converges to a specified tolerance value. A schematic of this algorithm is found in ***Figure 16***.

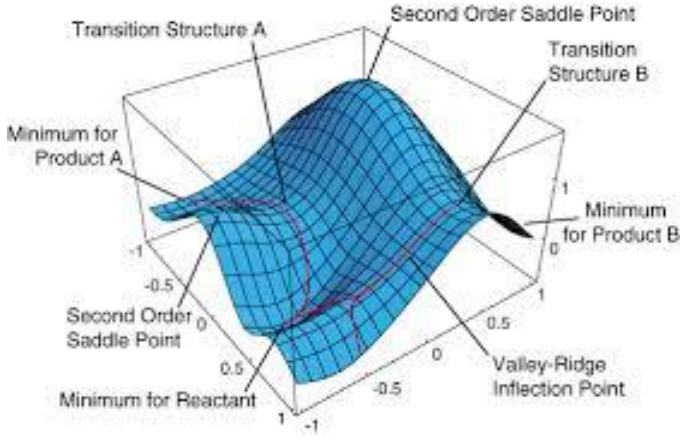


***Figure 15.*** An illustration of a potential energy surface.

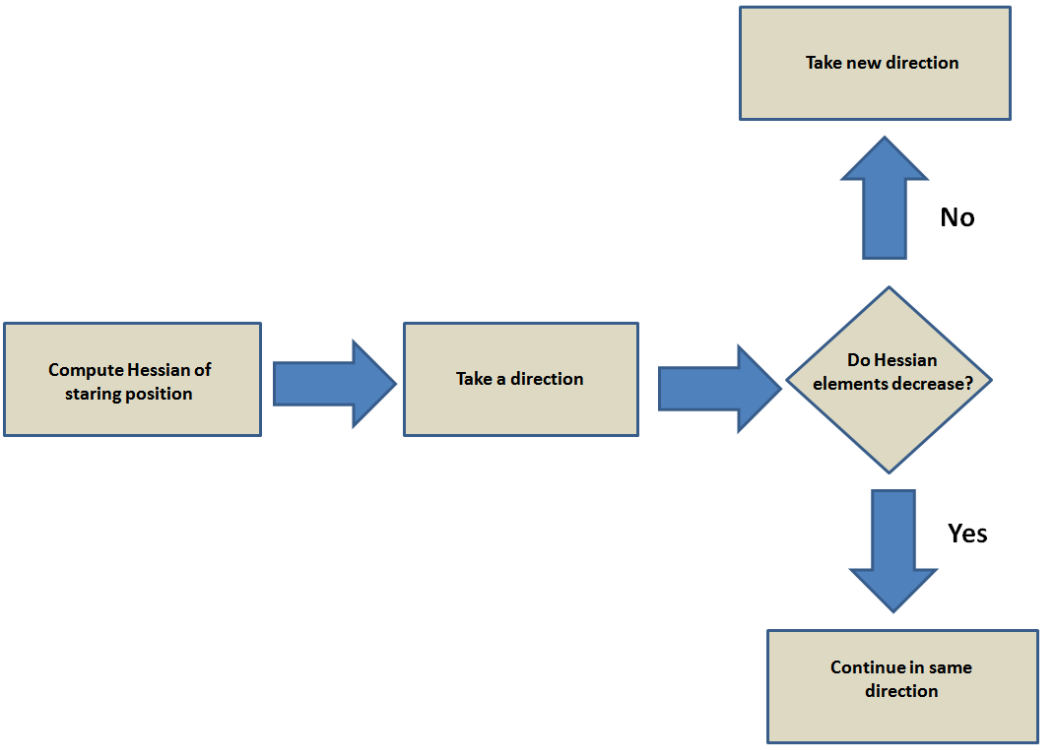


***Figure 16.*** A schematic of the steps present in the BFGS algorithm.

$$H(f) = \begin{bmatrix} \frac{\partial^2 f}{\partial^2 x_1^2} & \frac{\partial^2 f}{\partial x_1 \partial x_2} & \cdots & \frac{\partial^2 f}{\partial x_1 \partial x_N} \\ \frac{\partial^2 f}{\partial x_2 \partial x_1} & \frac{\partial^2 f}{\partial^2 x_2^2} & \cdots & \frac{\partial^2 f}{\partial x_2 \partial x_N} \\ \vdots & \vdots & \ddots & \vdots \\ \frac{\partial^2 f}{\partial x_N \partial x_1} & \frac{\partial^2 f}{\partial x_N \partial x_3} & \cdots & \frac{\partial^2 f}{\partial^2 x_N^2} \end{bmatrix} \quad (21)$$

## 3.3. The Quasi-Harmonic Approximation in Lattice Dynamics

To compute properties that depend on the dynamics of a system, physical phenomena such as temperature must be taken into consideration. In the case of calculations performed on a static lattice regime, the atoms are not allowed to move away from their equilibrium positions (associated with an energy minimum in the PES). At relatively low temperatures, the atoms are mostly just vibrating about their lattice sites, causing no substantial deformation to the whole molecular structure – low here is relative to the specific system. This scenario is best described by Quasi Harmonic approximation. Under this approximation, corrections are added to Hooke's model of a spring in order to give it a slight anharmonic character – hence the use of the expression "quasi-harmonic. The addition of this correction allows the atoms/ions to vibrate with respect to each other. As a result of this, the system is moving slightly away from its equilibrium position at the bottom of the energy potential well (global minimum in the PES). However, this model breaks down as one reaches the melting point of the system, whereby the atoms should have increased degrees of freedom. In this case other approximations may be used in this case.[57]

## 3.4. Bragg Coherence Diffraction Imaging

Imaging techniques have been widely used in a plethora of areas within the forum of scientific research. Examples of these techniques are microscopy and tomography. Microscopy is method whereby a lens is used to collect the light scattered by a sample with the aim of recovering an image. In spite of being widely used to reconstruct images of samples at the visible light wavelength scale, this technique suffers of some limitations when utilized with waves of wavelength in the x-ray region. The most common spatial resolution found at this level is of approximately 25 nm; which is rather far from the wavelength limit. A relatively recent new technique known as Coherent Diffraction Imaging (CDI) overcomes this problem by illuminating the sample with a coherent beam and scattering the light to a detector.

The work here discussed uses one of the five CDI techniques, known as Bragg Coherent Diffraction Imaging (BCDI).In this method a crystal (about 1 μm in size) is illuminated with x-rays (sourced by a synchrotron). The crystal is rotated about an axis until an angle that allows diffraction to occur (obeying Bragg's law) is procured. The successful find of an angle that obeys Bragg's condition, leads to a display of a Bragg peak on the detector. An illustration of this is depicted in ***Figure 17***.

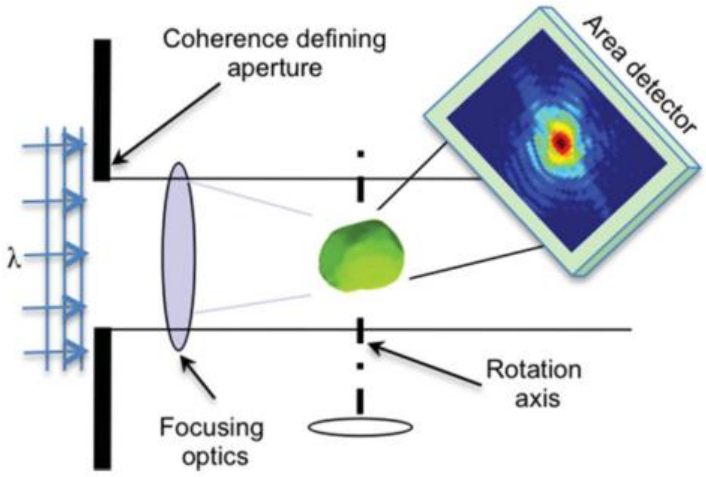


***Figure 17.*** A schematic of a BCDI set-up.[9]

In spite of CDI being able to overcome the wavelength limit problem highlighted previously, upon measuring the intensity of the scattered wave, its phase information is lost. This loss is a consequence of the phase being the imaginary party of the scattered wave in the Fourier transform of ***equation 22***. Since the measured intensity given by ***equation 23***, the imaginary part of ***equation 22*** disappears; where ρ is the phase, A is the amplitude of the scattered wave, I is the intensity, Q is the momentum transfer, V is the volume and r the distance. The loss of this information is formally known as the *phase problem*.

$$\vec{\rho} = \frac{1}{V}\int \tilde{A}(\vec{Q})e^{i\vec{Q}.\vec{r}}\,d^3\vec{Q} \qquad (22)$$

$$I = \left|\tilde{A}\right|^2 \qquad (23)$$

Once the diffraction pattern is obtained, the phase for the associated amplitude can be retrieved by using a number iteratively optimisation algorithms; namely the Error reduction (ER) and the Hybrid Input-Output (HIO) and algorithms. Relating back to the PES of ***Figure 15***, the purpose of the ER algorithm is to ensure that the optimisation always goes downhill whereas the HIO algorithm attempts to overshoot a current position of the a given step, allowing the optimisation to explore more of the PES and to avoid stagnation.

The diffraction data is inputted into the algorithm and an associated phase is randomly generated. This system is then reversed Fourier transformed to real space and a support is used to ensure that the phase outside the spatial region wherein the crystal is found. The system is subsequently Fourier transformed to reciprocal space. The newly formulated diffraction pattern (amplitude + generated phase) is then compared to the experimental diffraction pattern. The algorithm goes around in this cycle iteratively optimising the phase by increasing the level of similarity between the experimental diffraction pattern and the generated one. A summary of this process is summarised in ***Figure 18***.

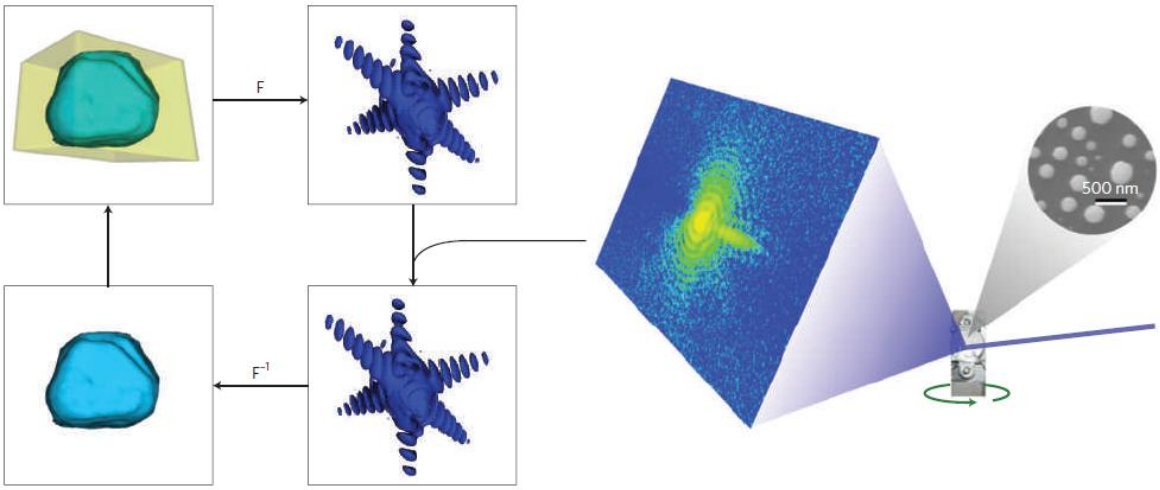


***Figure 18.*** An illustration of the HIO algorithm operation to obtain a 3D description of the crystal.[61]

The special trait of the BCDI method is that it allows one to map local structural strain information onto the reconstructed crystal. Consider the scheme of ***Figure 19***: on the top left-hand side one sees a perfect lattice wheretras on the bottom left-hand side one sees a defected one. The displacement field vector, u (a Burgers vector), represents how a given point in that lattice has changed spatially; refer to ***equation 24***, where r is the position and $r_o$ the initial position of a given lattice point in the lattice. Once a converged diffraction pattern is found, with the process discussed previously, the strain information may be computed by making using of two relationships. Firstly, the fact that the phase is proportional to u. Lastly, the strain tensor is related to the deformation by the antisymmetric differential seen in ***equation 25***; where ε refers to the strain, and $x_j$ represents the spatial coordinate in the orthogonal direction j. The reader is referred to ***Figure 20*** for an example of what the three dimensional reconstruction of a crystal morphology and mapped strain, in this case for barium titanate, looks like.

$$\vec{u}(r) = r - r_o \qquad (24)$$

$$\underline{\underline{\varepsilon}}_{ij} = \left(\frac{d\vec{u_i}}{dx_j} - \frac{d\vec{u_j}}{dx_i}\right) \qquad (25)$$

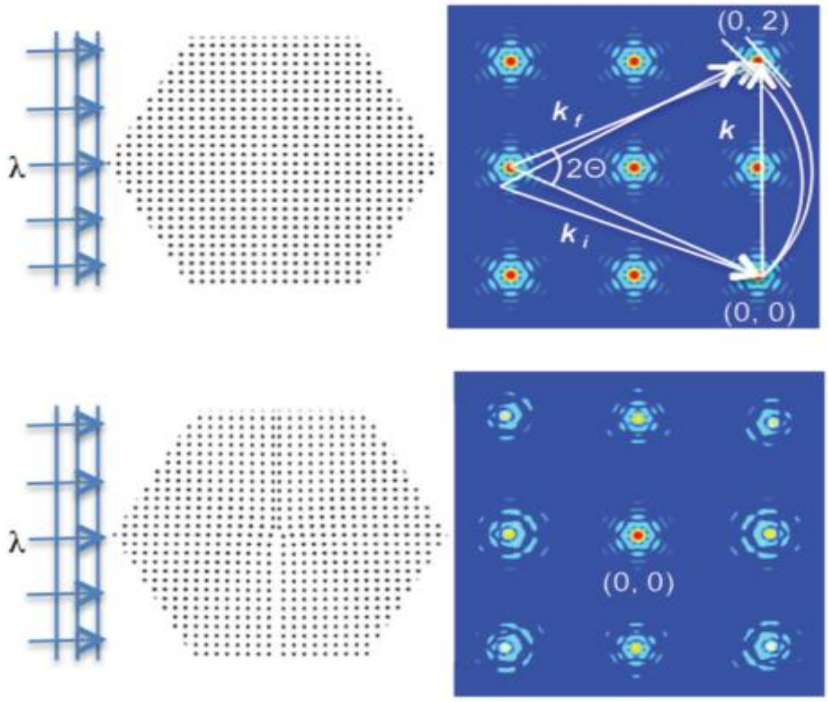


***Figure 19.*** A schematic of the effect of structural distortion on the shape of the diffraction pattern.[9]

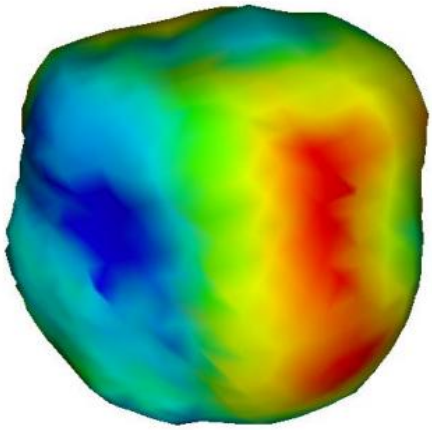

***Figure 20.*** A three dimensional reconstruction of a barium titanate crystal. The contouring reflects the relative different amounts of strain around the crystal.

# *Chapter IV*

# *Methodologies*

In the course of this investigation both molecular modelling and imaging techniques have been applied in order to gain some insight as to why Cu/SAPO-34 shows low hydrothermal stability.

## 4.1. Molecular Modelling

GULP, version 3.4, was used to compute all the different properties of the modelled AlPO-34 and SAPO-34 systems.[62] This code uses standard techniques based on the Ewald method (see ***Chapter III***). The AlPO-34 structure, obtained from the crystallographic database, was used as the starting point to build all the H/SAPO-34 and Cu/SAPO-34 models.[63] All the models, which were based on a 2x2x2 super cell of the original unit cell for each model, were allowed to relax without symmetry constraints and under pressure conditions (0 GPa). The BFGS minimisation technique (**Chapter III***)* was utilized in all the calculations and a convergence criterion for the gradient norm below 0.0001 $eVÅ^{-1}$ was thought to be appropriate.

The interatomic potentials used to model the interactions between the ions in the structure included the following terms: Coulombic interactions, short-range pair potentials (described by a Buckingham potential function – as discussed in ***Chapter III***), and a three body, bond bending term. A cut-off distance of 16Å was used for the short-range interactions. The shell model (refer to ***Chapter III***) was used to simulate the polarizability of the $O^{2-}$ ions. The potentials used in this study were those also used by Sastre *et al*.[64]

AlPO-34 and H/SAPO-34 were used in this study to be used as a 'controls' for the analysis of the Cu/SAPO-34 results (*e.g.* H/SAPO-34 was used to analyse the SAPO-34 system without the presence of Cu).

The Si distribution used in all the models was based on the *isolated* Si distribution described in ***Chapter II***. A two dimensional illustration of this distribution is presented in ***Figure 21*.** The Si composition was allowed to vary between 0 % and 8.4 %. This maximum value was to used to ensure that the models was relatively far away from the 10 % threshold beyond a regime where Si *islands* become dominant.

H/SAPO-34 was assessed during the static lattice calculations with respect to having the $H^+$ extra-framework ion present at all the crystallographically distinct oxygens, referred in this work as O1, O2, O3 and O4. The Cu ions in Cu/SAPO-34 was modelled only at the 8MR (analogous to site IV in ***Figure 4***).

During the lattice dynamics calculations, used for the NTE prediction, the system was sampled at the Γ point in a 3x3x3 *k*-point mesh. The systems were evaluated at a temperature range between 0 K and 500 K in and the associated phonon density of states (DOS) subsequently computed.

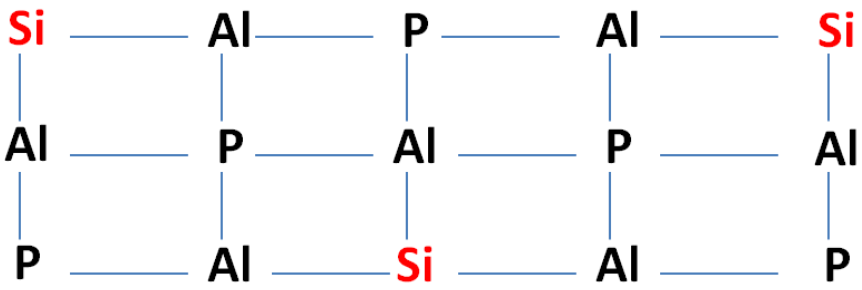


***Figure 21.*** A two dimensional representation of the *isolated* Si distribution used in SAPO-34 models.

## 4.2. SAPO-34 samples

The SAPO-34 and Cu/SAPO-34 samples were supplied by JM (JM-SAPO-34 and JM-Cu/SAPO-34, respectively). In order to adhere the sample to the surface of a Si wafer and to the inner walls of a glass capillary (2mm diameter), the sample was mixed with 5 ml of ethanol and 10 ml of tetraethyl orthosilicate (TEOS)– the former to dilute the powder and the latter to ensure that crystals remained on the surface of the Si wafer and in the capillary (2 mm in diameter). The yielded solution was sonicated for 10 min and subsequently added, drop wise, to the surface of the silicon wafer and into the capillary. The samples were subsequently heated up at a temperature of 100 $^{o}$C for 2 hours. The samples were then mounted onto a piezo stage. For the purposes of the capillary experiment, the tube was connected to a heated water bath at approximately 50 $^{o}$C that was also connected to a supply of $N_2$ gas. A schematic of the set-up is illustrated on ***Figure 22.***

## 4.3. Powder X-ray Diffraction

The powder x-ray diffraction (PXRD) study was performed by using Cu-$K_{\alpha 1}$ radiation (using 40kV and 30 mA) of wavelength 1.54 Å. The Cu/SAPO-34 was introduced into a capillary and analysed using a Stoe STADI-P instrument by measuring a range of angles between $0^0$ and $59.895^o$ in steps of $0.495^o$ at 10 seconds per step. The sample was heated up to a temperature of 500 K and cooled down to 100 K in 10 K steps.

## 4.4. BCDI

The BCDI experiments were performed both in the Advanced Photon Source and in the Diamond Light Source:

Focused coherent x-rays with a wavelength of 0.1378 nm from the 34-ID-C beamline in the Advanced Photon Source illuminated the SAPO-34 samples both on the silicon wafer and within a 2 mm diameter capillary. The coherent x-ray diffraction patterns were measured using a charge-coupled device (CCD) detector with 55 $\mu m^2$ pixels located 1.6 m away from the sample.

Focused coherent x-rays with a wavelength of 0.13625 nm from the I-13 beamline in the Diamond Light Source illuminated the SAPO-34 samples both on the silicon wafer and within a 2mm diameter capillary. The coherent x-ray diffraction patterns were measured using a CCD detector with 55 $\mu m^2$ pixels located 2.7 m away from the sample.

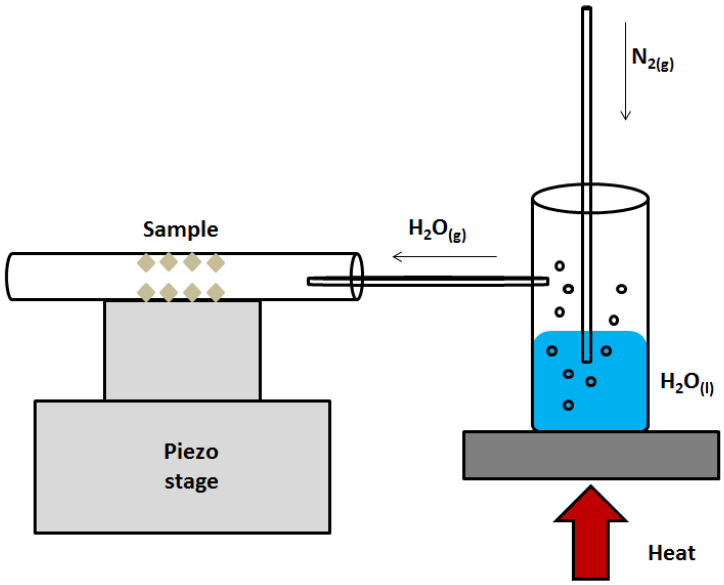


***Figure 22.*** A schematic of the experimental set-up used in the Diamond Light Source to assess the effect of $H_2O$ vapour on the strain pattern of Cu/SAPO-34 crystals.

# *Chapter V*

# *Results and Discussion*

## 5.1. Geometry optimisation of AlPO-34

The geometry optimised AlPO-34 framework was compared to that published by Sastre and co-workers.[64] The reader is pointed to ***Table 1***, where the various measured bond distances, bond angles and lattice energy obtained in this study, along with those obtained by Sastre and Ito *et al*. (PXRD) are found.[64,63] The nomenclature used on this table is related to the atoms seen in ***Figure 22***.

The lattice energy from the optimised AlPO-34 was very close to that of Sastre; 0.001 eV higher in energy. This disparity was justified with the slight differences in versions of GULP that may lead to a slight different protocol in the optimisation process. It was proposed that a difference of this magnitude divulges a high degree of confidence on the geometry of the optimised AlPO-34 framework; assuming that Sastre's structure is found at the global minimum of the PES.

With regards to the bond distances this work's values were slightly different from Sastre's. This was mostly probable due to the fact that this investigation's AlPO-34 structure is found at a different point of the PES. Although the structures are energetically very similar, small differences in the energy may lead to rather more pronounced disparities in the structure. This argument also applies for the case of the bond angles. A much larger difference from Sastre's AlPO-34 was seen here, however the same point should apply.

When compared to Ito's work, it was concluded that there was some level of discrepancy between the theoretical values (this work's and Sastre's) achieved to those yielded via PXRD. The magnitude of this difference for each one of the two of the modelling studies may be seen under the respective "error" column; whereby the absolute difference between theory and experiment was calculated. Overall, the "errors" were found to be very similar to each other; again a bit more pronounced when it comes to the bond angles.

In the light of the results obtained and tabulated on ***Table 1*** and the arguments given above, it was established that this optimised AlPO-34 framework was good enough to use as a starting point for the subsequent SAPO-34 models.

***Table 1*** **|** The values from the geometry optimisation of AlPO-34 from this study and how they compare with the work of Sastre and Ito.[64,63]

| | Lattice Energy / eV |
|---|---|
| **Current** | -267.979 |
| **Sastre**[64] | -267.980 |

| | Lattice Parameters | | | | |
|---|---|---|---|---|---|
| | **Current** | **Sastre**[64] | **Ito**[63] | **error Current** | **error Sastre** |
| ***a* = *b* = *c*** | 9.291 | 9.290 | 9.370 | 0.08 | 0.08 |
| ***α* = *β* = *γ*** | 94.94 | 94.84 | 94.68 | 0.26 | 0.16 |

| | Distances / Å | | | | |
|---|---|---|---|---|---|
| | **Current** | **Sastre**[64] | **Ito**[63] | **error Current** | **error Sastre** |
| **P-O(1)** | 1.524 | 1.522 | 1.504 | 0.020 | 0.018 |
| **P-O(2)** | 1.508 | 1.509 | 1.595 | 0.087 | 0.086 |
| **P-O(3)** | 1.528 | 1.526 | 1.508 | 0.020 | 0.018 |
| **P-O(4)** | 1.509 | 1.511 | 1.600 | 0.091 | 0.089 |
| **O(1)-Al(1)** | 1.716 | 1.720 | 1.691 | 0.025 | 0.029 |
| **O(2)-Al(2)** | 1.726 | 1.724 | 1.722 | 0.004 | 0.002 |
| **O(3)-Al(3)** | 1.721 | 1.724 | 1.752 | 0.031 | 0.028 |
| **O(4)-Al(4)** | 1.734 | 1.731 | 1.676 | 0.058 | 0.055 |

| | Angles / $^{o}$ | | | | |
|---|---|---|---|---|---|
| | **Current** | **Sastre**[64] | **Ito**[63] | **error Current** | **error Sastre** |
| **PO(1)Al(1)** | 150.72 | 149.50 | 151.20 | 0.48 | 1.7 |
| **PO(2)Al(2)** | 147.96 | 147.80 | 144.30 | 3.66 | 3.5 |
| **PO(3)Al(3)** | 147.80 | 147.60 | 147.40 | 0.4 | 0.2 |
| **PO(4)Al(4)** | 142.41 | 142.80 | 146.10 | 3.69 | 3.3 |

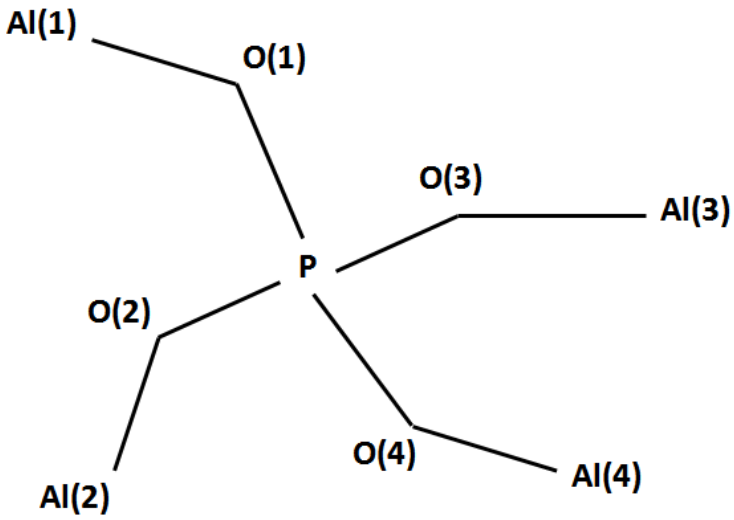


***Figure 23***. A depiction of the framework used to define the nomenclature used on ***Table 1***.

## 5.2. Structural consequences of $P^{5+}$ to $Si^{4+}$ substitution in the SAPO-34 framework

During the process of doping AlPO-34 with $Si^{4+}$ and the respective extra-framework ion, it was questioned what the extent of structural distortion would be for the whole SAPO-34 framework. To answer this question, the bond length between the doped Si and each one of the four crystalographically distinct oxygens was measured. An average of those measured values was taken and the absolute difference between that averaged values and the averaged value for the P-O bond distances in AlPO-34 was computed. This difference is seen in ***Figure 24***, at $\rho = 0$. The same calculation was done for every first near neighbouring P ions to that Si, an average of the bond distances of all these P atoms were computed and the same deduction was performed as discussed before. In this case the value for this difference is found at $\rho = 1$. This computation of the averaged absolute differences were done for the $2^{nd}$ ($\rho = 2$) and $3^{rd}$ ($\rho = 3$) too. The results showed a exponential type decay revealing that the distortion only really happen very close to the Si site.

As it will become apparent in the next subsection, these local distortions have consequences in the overall symmetry of the modelled SAPO-34 super cell.

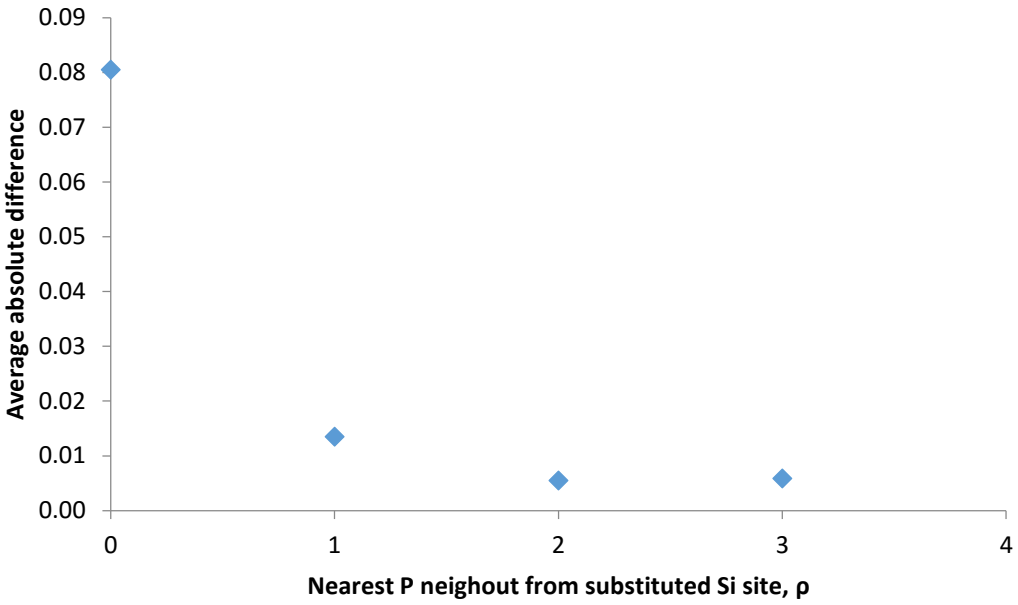


***Figure 24.*** A graphical representation of how the average difference of Si-O and each P-O different in H/SAPO-34 from AlPO-34.

## 5.3. Static lattice results for H/SAPO-34 and Cu/SAPO-34

In order to establish whether the models were structurally coherent, the lattice parameters and the unit cell volume were plotted as a function of the content of Si. It was believed that, if they followed Vegard's law, this would be an indication that they were structurally consistent.

For the case of H/SAPO-34 (***Figure 25***), as the content of Si increased, there was an overall enlargement of the unit cell in both cases. This unit cell expansion is predictable since the occupied volume by the extra-framework ion and a $Si^{4+}$ is larger than that of $P^{5+}$. The expansion of the unit cell volume is linear for all the crystallographically distinct oxygens; which agrees with Vegard's law. However, in spite of the predictability of the obtained results, the lattice parameters we found to show non-linear correlations with the Si content across the different oxygens. It was suggested that this non-linear correlations had arisen due to a break in the symmetry of the unit cell. As it was brought to light in ***Chapter II***, SAPO-34 has rhombohedral symmetry (space group $R\bar{3}m$). Since GULP calculates the properties of the models in a periodic fashion, any defects that are introduced into a unit cell (or to a super cell), are propagated throughout space in a periodic manner. As a result, the calculation

breaks down the symmetry of the H/SAPO-34 from the original $R\bar{3}m$ found in AlPO-34 to a *P1* (the lowest symmetry possible). It was postulated that this break of symmetry was a result of, not only the present of the defect but also due to the distortions featured measured and depicted in ***Figure 24***. The retention of higher order of symmetry by the real system may arise because the distribution of Si throughout the crystal will be such as to ensure to be found at the highest possible entropic state. Consequently, the symmetry distinct positions of each Si in the real material will 'cancel out' giving rise to a preservation of the $R\bar{3}m$ symmetry.

In an attempt to solve this problem, it was assumed that the symmetry of the unit cell could be approximated to the $R\bar{3}m$ values by computing the geometric average of the lattice parameters for each concentration and for each oxygen atom. The volume, *V*, of the rhombohedral cell was calculated by inputting the averaged lattice constants into ***equation 26***; where *A* denotes the length of the rhombohedral cell and α its angle.

$$V = A^3\sqrt{1 - 3cos^2\alpha + 2cos^3\alpha} \quad (26)$$

The plots of how the lattice parameters *A* and α and the unit cell volume for this approximation are illustrated in ***Figure 26***. As expected, *A* varied linearly with the Si content and so does the unit cell volume. The angles, varied in a more random manner, however they remained very much constant with increased amounts of Si being inserted into the SAPO-34 framework. Since the results from this 'correction' seemed reasonable, this approach was taken used for Cu/SAPO-34 case as well.

The lattice energy was found to vary linearly with the insertion of $Si^{4+}$ and $H^{+}$. By using linear regression analysis, it was found that the result predicted an energy of 0.59 eV per $Si^{4+}/H^{+}$ substitution. The literature was explored but no publication was found with a result that could be used to compare.

Since the Vegard's Law prediction worked very well for H/SAPO-34, it was concluded that the same type work would not have to be conducted for Cu/SAPO-34 because, the lattice expansion occurring by virtue of the insertion of a larger substituent into the system, should be independent of extra-framework ion.

The tabulated values for the 'as-modelled' H/SAPO-34 and 'corrected' H/SAPO-34 maybe found in ***Appendices 1*** and ***2***, respectively.

.

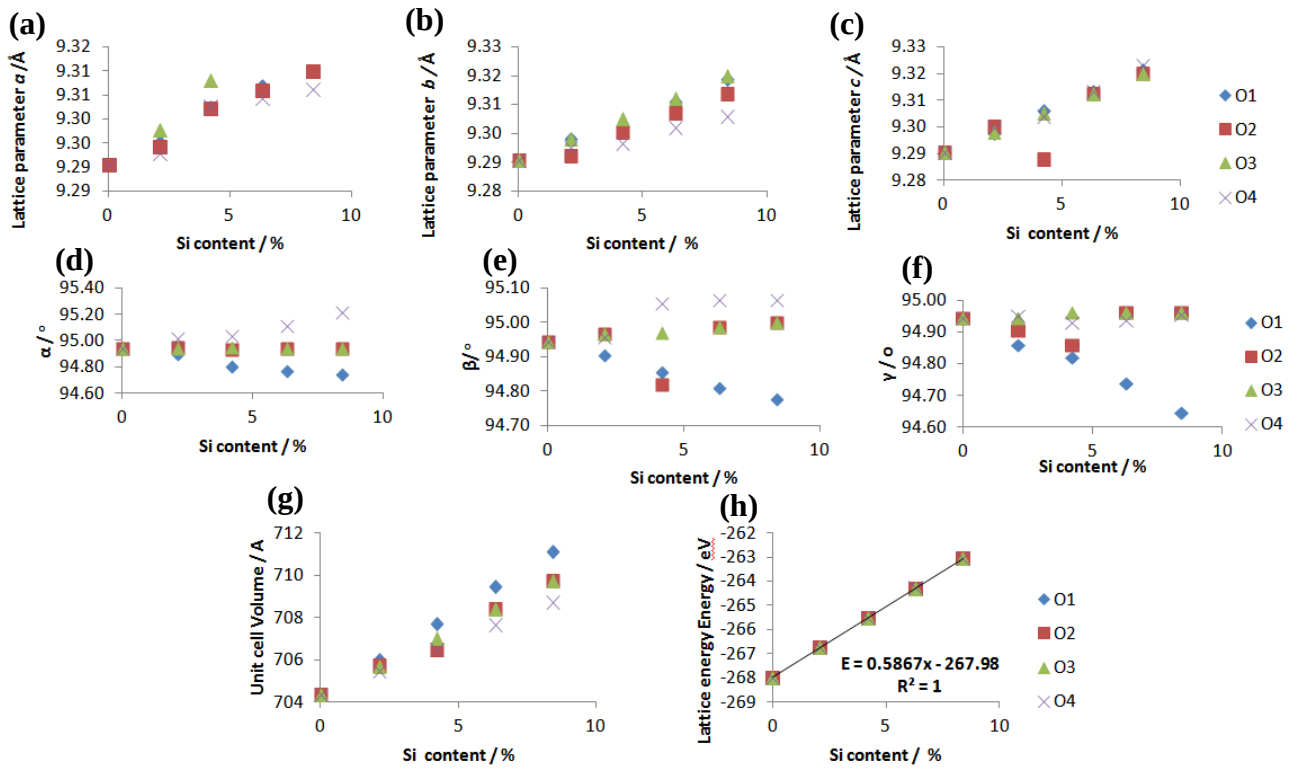


**Figure 25.** An illustration of (*a)* the lattice parameter *a*, (*b)* the lattice parameter *b*, (*c)* the lattice parameter *c*, (*d)* the lattice parameter *α*, (*e)* the lattice parameter *β*, (*f)* the lattice parameter *γ*, (*g)* the unit cell volume and (*h)* the lattice energy as a function of the Si content for H/SAPO-3. O1, O2, O3 and O4 denote the four crystallographically distinct oxygens.

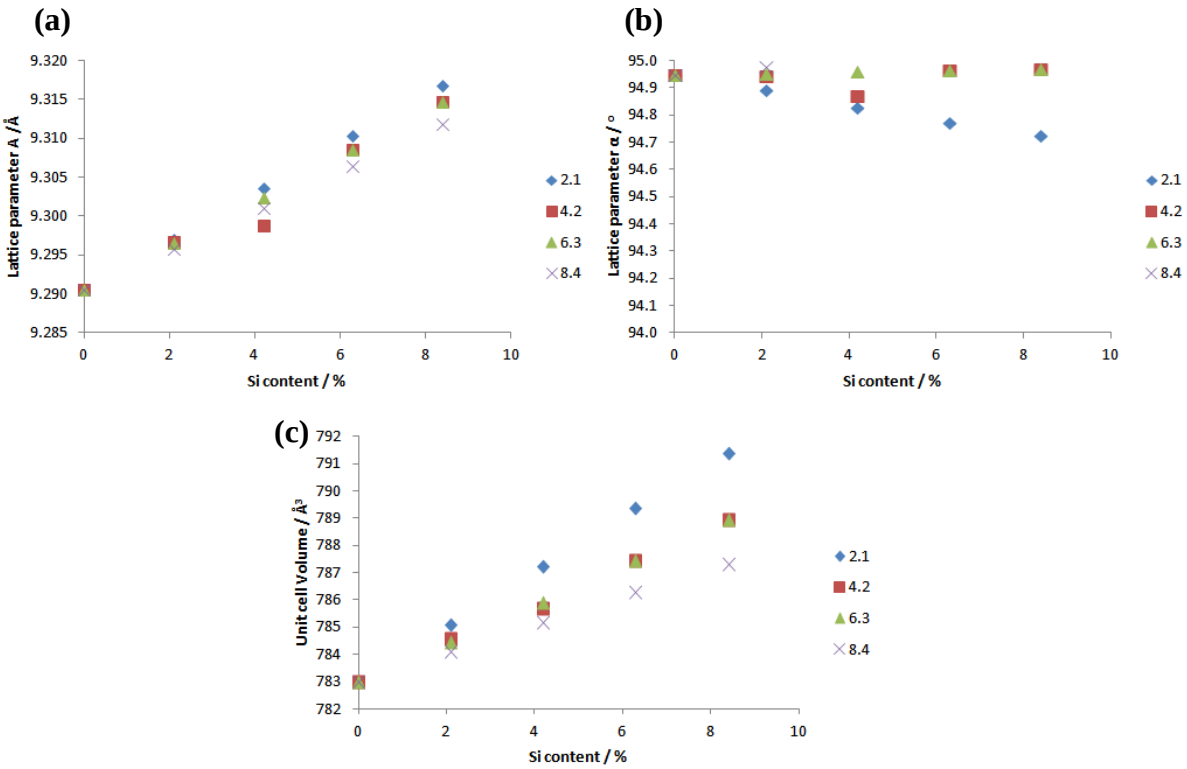


***Figure 26.*** The graphical representation lattice parameters *A (a)* and *α (b)* and unit cell volume (c) as function of the Si for H/SAPO-34 upon using the geometric average approach to overcome the problem of symmetry breaking.

## 5.4. NTE prediction of AlPO-34, H/SAPO-34 and Cu/SAPO-34

The results from the lattice dynamics calculation for the AlPO-34 model are illustrated in ***Figure 27.*** Taking into account that the lattice parameter *A* and the unit cell volume decreased as a function of the temperature and that α did not change, it was concluded the AlPO-34 was predicted to display NTE behaviour between 0 K and 500 K. No data was found in the literature to compare these results, neither computational nor experimental. By making use of ***equations 6*** and ***8***, $\alpha_l$ and $\alpha_V$ were calculated (see ***Table 2***)

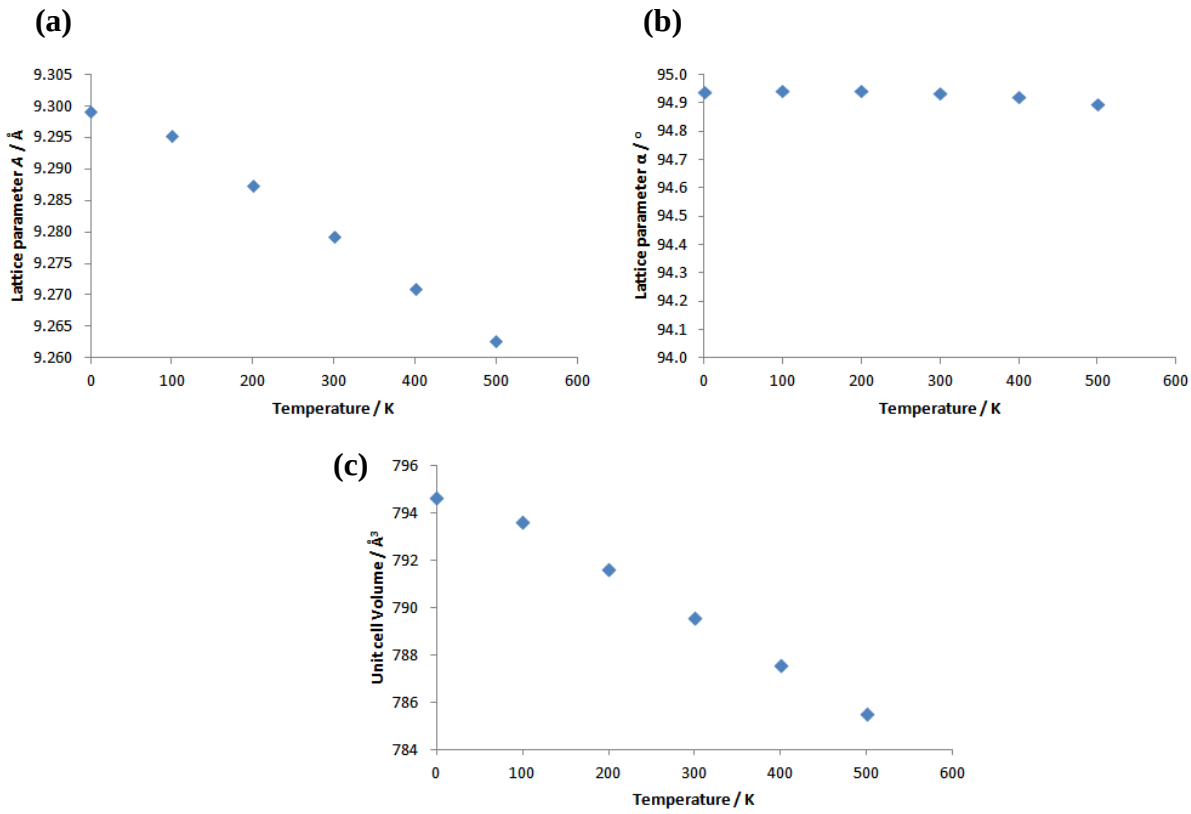


***Figure 27.*** The successful prediction for NTE behaviour of AlPO-34, as the lattice parameters A (*a*), α (*b*) and (*c*) the unit cell volume decrease as a function temperature.

In the case of H/SAPO-34(***Figure 28)***, the results also revealed that the lattice parameters and the unit cell volume contracted as a function of the temperature. The change in the lattice constant α was small in comparison and the net change of α over this 500 K range was found to be almost zero. It was concluded that the calculations predicted NTE behaviour for H/SAPO-34 within the investigated temperature range. By making use of ***equations 6*** and ***8***, $\alpha_l$ and $\alpha_V$ were calculated (see ***Table 2***).

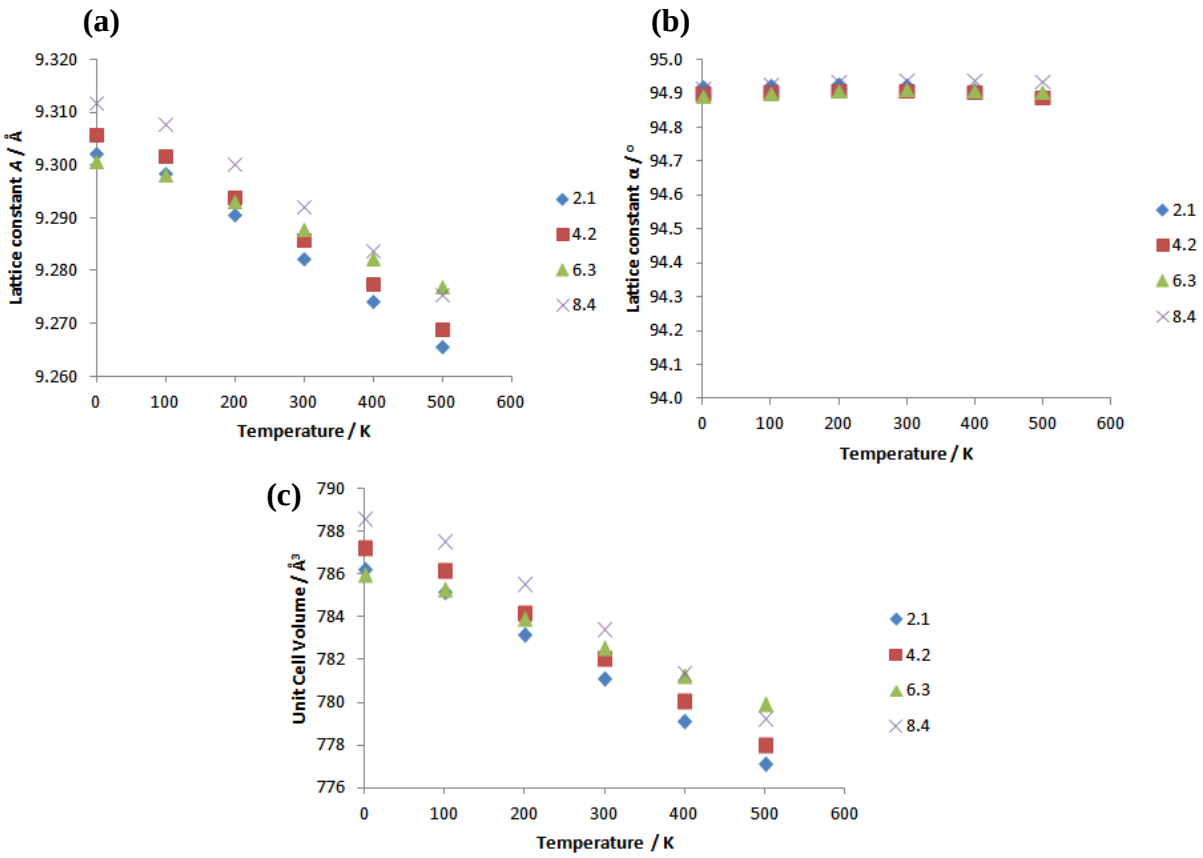


***Figure 28.*** The successful prediction for NTE behaviour of H/SAPO-34, as the lattice parameters A (*a*), α (*b*) and the unit cell volume decrease as a function temperature. The different colour on the data points represent the different concentration of Si probed in the model.

Finally, Cu/SAPO-34 (***Figure 29***) was also found to display NTE within the same temperature, for the same arguments used above. The graphs depict the prediction for Cu/SAPO-34 only with $Cu^{1+}$. This was true for all the most energetically favourable configuration of the system with respect to the number of Cu ions and their oxidation states. By making use of ***equations 6*** and ***8***, $\alpha_l$ and $\alpha_V$ were calculated (see ***Table 2***).

The tabulated values that gave rise to the plots of ***Figures 27, 28*** and ***29*** may be found in ***Appendices 3***, ***4*** and ***5***.

The values of α (***Table 2***) increase for all the models as a function of the composition of Si at a steady rate, except when Si molar fraction 6.2 % is reached. Overall, larger amounts of Si seem to slow down the rate not NTE.

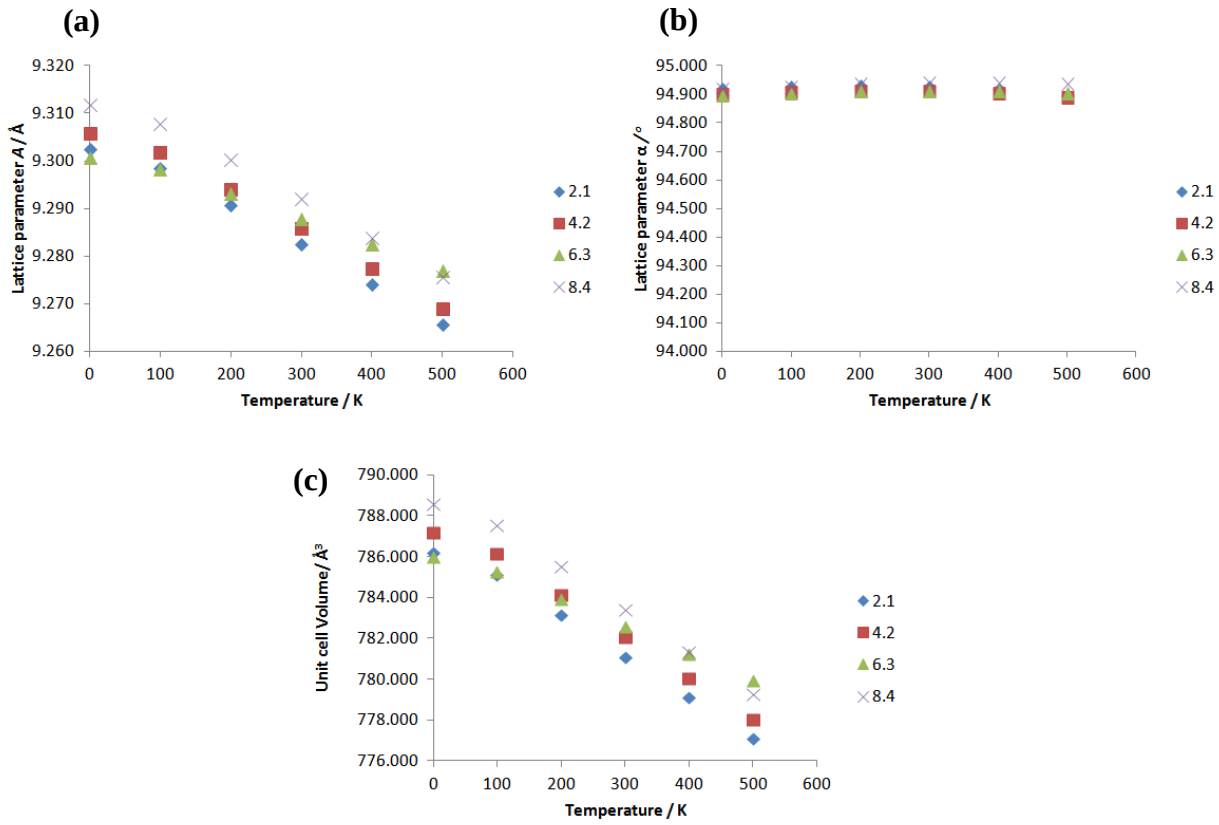


***Figure 29.*** The successful prediction for NTE behaviour of $Cu^{+}$/SAPO-34, as the lattice parameters A (*a*), α (*b*) and the unit cell volume decrease as a function temperature. The different colour on the data points represent the different concentration of Si probed in the model.

## 5.5. The mechanism behind the NTE behaviour in AlPO-34, H/SAPO-34 and Cu/SAPO-34

When zoomed-in within the *near-zero* frequency, the results from the phonon DOS revealed an increased in the number occupied states as a function of the temperature. The phonon DOS of ***Figure 30*** are those related to H/SAPO-34. The same result was obtained for AlPO-34 and for Cu/SAPO-34. This result clearly shows that RUMs, the mechanism introduced in ***Chapter II***, is the mechanism via which the NTE behaviour is taking place in all three systems.

***Table 2*** **|** The tabulated values of $\alpha_l$ and $\alpha_V$ for AlPO-34, H/SAPO-34 and Cu/SAPO-34 at different compositions of Si.

| Si % | AlPO-34 | | H/SAPO-34 | | Cu/SAPO-34 | | | | | |
|---|---|---|---|---|---|---|---|---|---|---|
| | | | | | $Cu^+$ only | | Mixed | | $Cu^{2+}$ only | |
| | $\alpha_l$ / $K^{-1}$ | αv / $K^{-1}$ | $\alpha_l$ / $K^{-1}$ | αv / $K^{-1}$ | $\alpha_l$ / $K^{-1}$ | αv / $K^{-1}$ | $\alpha_l$ / $K^{-1}$ | αv / $K^{-1}$ | $\alpha_l$ / $K^{-1}$ | αv / $K^{-1}$ |
| **0** | -7.8E-06 | -2.4E-05 | | | | | | | | |
| **2.1** | | | -7.9E-06 | -2.4E-05 | -7.9E-06 | -2.4E-05 | | | | |
| **4.2** | | | -7.9E-06 | -2.4E-05 | -7.9E-06 | -2.4E-05 | | | -7.9E-06 | -2.4E-05 |
| **6.3** | | | -5.1E-06 | -1.5E-05 | -5.1E-06 | -1.5E-05 | -6.9E-06 | -2.1E-05 | | |
| **8.4** | | | -7.8E-06 | -2.3E-05 | -7.8E-06 | -2.3E-05 | -7.2E-06 | -2.2E-05 | -7.0E-06 | -2.1E-05 |

## 5.6. PXRD results for JM-CU/SAPO-34

To assess whether JM-Cu/SAPO-34 displayed NTE behaviour, a powder x-ray diffraction investigation of the impact of temperature on the yielded diffractogram. The results are illustrated in ***Figure 31***. By comparing the yielded diffractogram of ***Figure 31a*** to that published by Martínez-Franco *et al.*[18] (illustrated in ***Figure 5***) one realises that the 2θ values were very the same. Also after a close look at the higher order peaks, see ***Figure 31b***, it is clear that there is a shift of the peaks with relation to each as a function of the temperature. Upon using Lebail refinement, it was concluded that lattice parameters of the JM-Cu/SAPO-34 were $A$ = 9.37 Å and 9.36 Å for 300 K and 490 K, respectively and an α of 94.3 $^{o}$ for both temperatures. These values are slightly different from those obtained for AlPO-34 (**Appendix 3**), H/SAPO-34 (**Appendix 4**) and Cu/SAPO-34(**Appendix 5**), when comparing 300 K and 490 K, from the PXRD experiment, with the 500 K data from the modelling work. Two reasons may be at the heart of this difference: *(i*) the fact that the potentials used for the modelling work may not predict the NTE behaviour with great level of accuracy, since some electronic effects may also play a role; interatomic potentials neglect electronic effects; (*ii)* the fact that models themselves were not close to the sample; that is, different Si distribution (possible presence of Si *islands*, which was not modelled here), or different Cu site (here only modelled for 8MR coordination). Or even perhaps, a mix of all these factors.

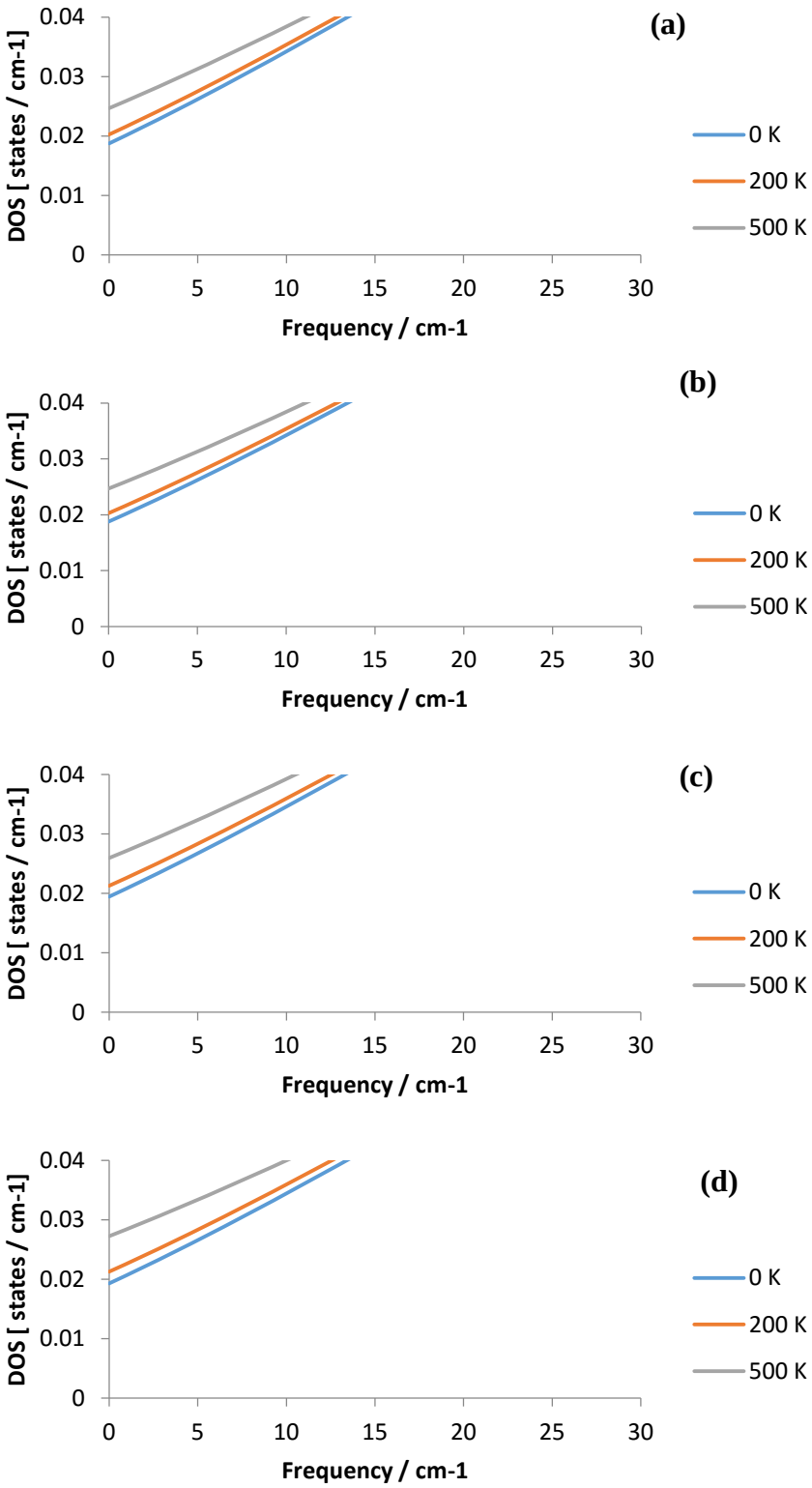


***Figure 30.*** The phonon DOS of H/SAPO-34 at 0 K (blue), 200 K (orange) and 500 K (grey), ***(a)- (d)*** represent the composition of 2.1%, 4.2%, 6.3%, 8.4% Si, respectively.

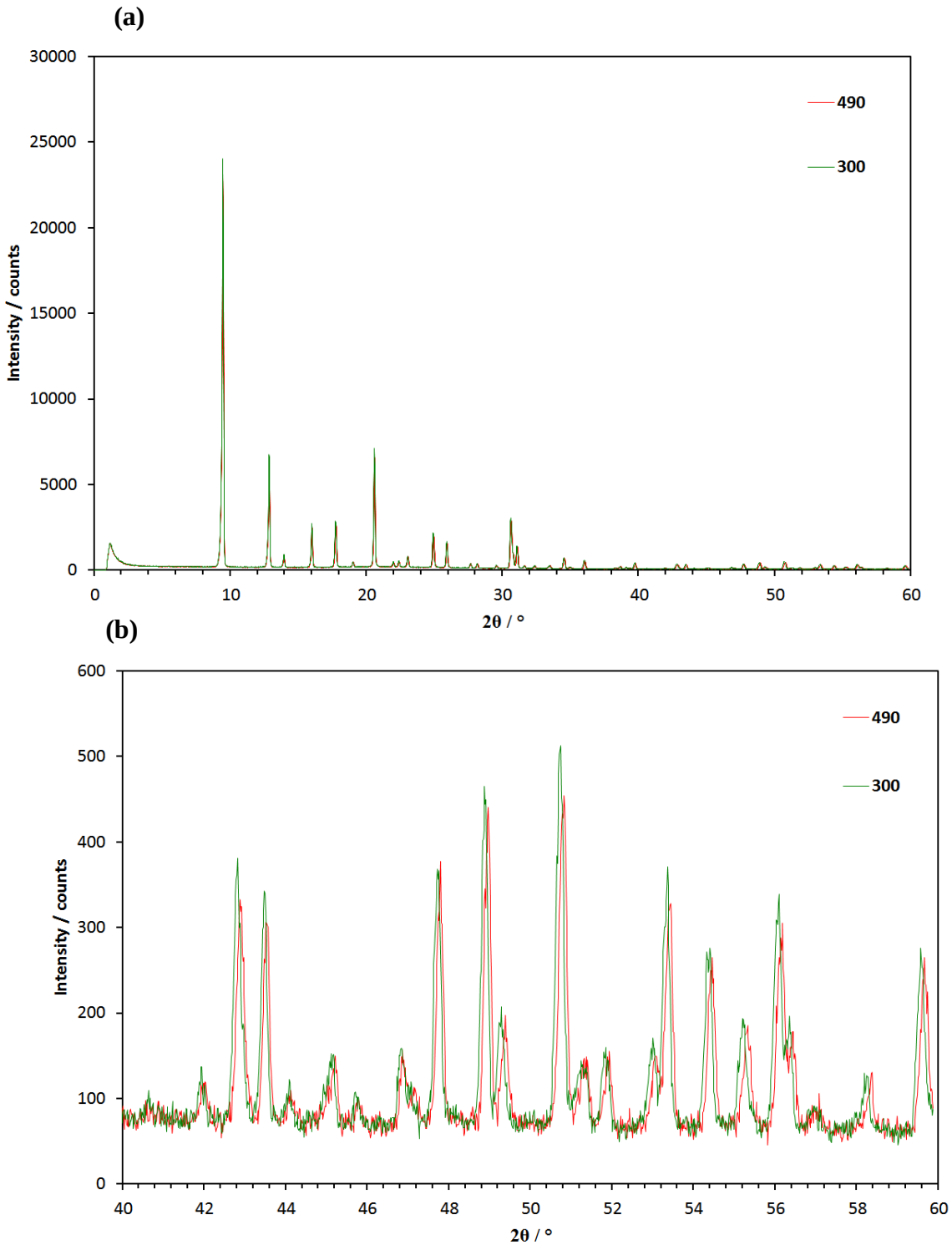


***Figure 31.*** The diffractograms of Cu/SAPO-34 for the temperature of 490 K (red) and 300 K (blue) *(a*) and (*b)*.

## 5.7. BCDI results

### 5.7.1. Samples on Si wafer

Two different samples of SAPO-34 powder were analysed whilst on a Si wafer: JM-SAPO-34 (SAPO-34 with no copper ions, provided by JM), JM-Cu/SAPO-34. The results obtained for a crystal of each one of these samples is seen in ***Figure 32a*** and ***b***. As it was previously discussed in ***Chapter 2***, SAPO-34 crystal have been studied via SEM and it has been concluded that these crystals show a rather regular cubic shape.[19] In spite of this, the BCDI reconstructions always yielded an amorphous shape, quite distinct from what is obtained in the SEM experiment. It was postulated that this distinction may have arisen due to a number of reasons: (*i*) the fact that SAPO-34 may not have long-range order throughout the whole crystal. This means that upon performing the diffraction studies on such samples, the obtained results are only related to the portion of SAPO-34 crystal that has long0range order. Again, as highlighted in ***Chapter 2***, there has been some speculation regarding the presence of stacking faults in the SAPO-34 structure.[20] If these faults were to be found only at some places in the crystal, perhaps as a result of the synthesis technique, they would contribute to the breaking of symmetry in specific areas in the crystal. *(ii*) The phase retrieval algorithm may not have converged to a result that corresponds to the 'true' solution. It may be that the algorithms used (HIO and ER – see ***Chapter III***) to find the global minimum in the configuration landscape of this problem are not very successful. They may work for very systems that have simpler landscapes (ones with only one or a just a few minima), or for cases when the collected diffraction pattern is of very high quality; which a lot of the time it was not the case with this experiment. *(iii)* A mixture of both cases may have contributed to it. However, taking into account that this amorphous shape was obtained for the two samples and for more than one crystal (*i.e.* more than one diffraction pattern***)***, it may be likely that this result is real and that SAPO-34 does indeed have domains in its crystal structure that are more crystalline than others.

Moreover it was also found that in the two samples is the fact that the mapped phase (and thus the strain) was quite homogenous throughout the entire reconstructed object. Thus, at least for the portion of the SAPO-34 crystal that can be reconstructed via BCDI, room temperature SAPO-34 does not seem to be strained in any way – as predicted, since the

hypothesis was that strain would arise as a result of the temperature and water content (not hydrothermally stable).

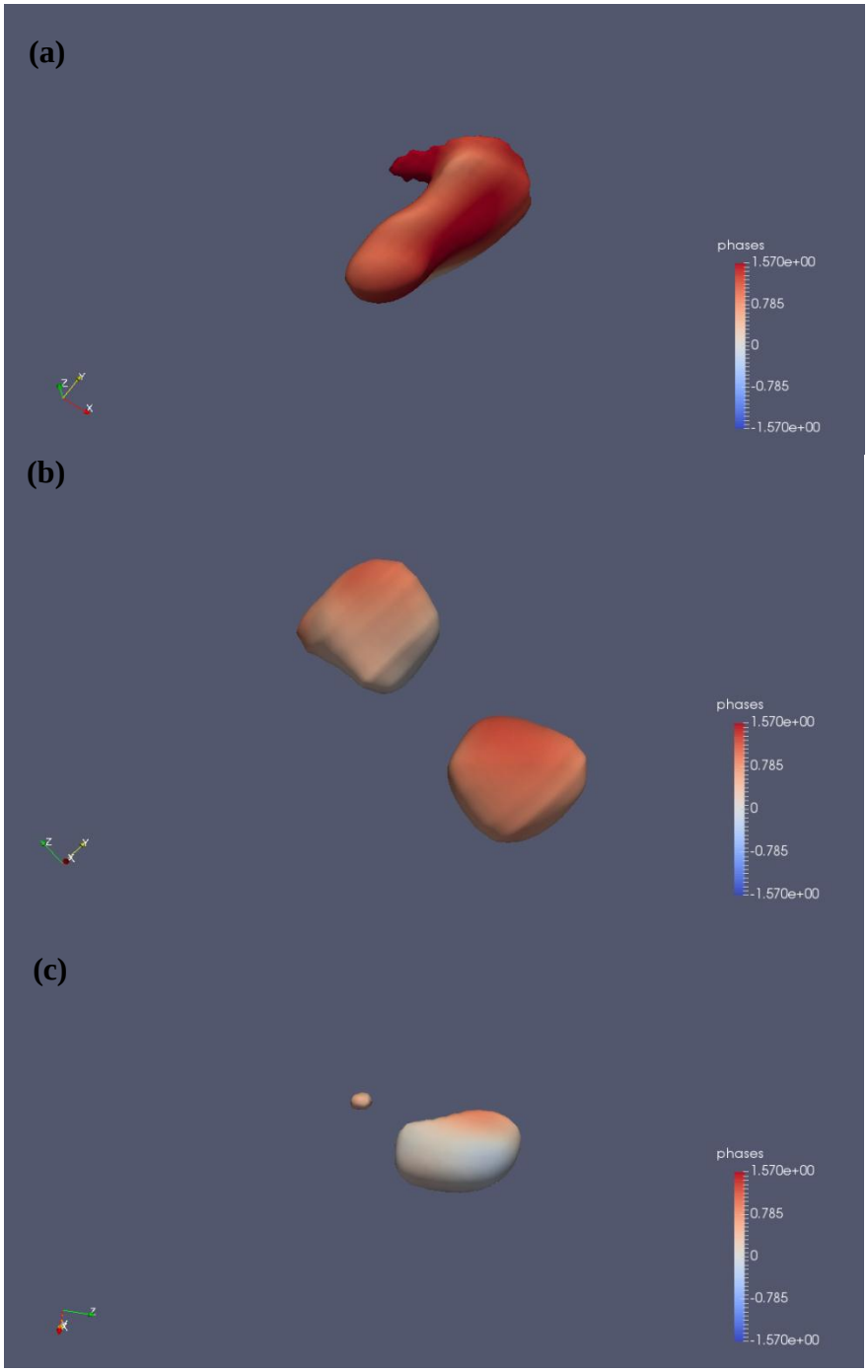


***Figure 32.*** The three dimensional reconstructions of ***(a)***JM-SAPO-34 on a Si wafer, ***(b)*** *Cu/SAPO-34 on a Si wafer and* **(c)** *JM-SAPO-34 in a capillary.*

### 5.7.2. JM-SAPO-34 in capillary at ambient conditions

Along with adding the two SAPO-34 samples onto a Si wafer, with the aim of having a set-up that allowed for the flow of gas, the samples were also introduced into a capillary. At first the samples were analysed at room temperature with no gas flowing. The obtained reconstruction for JM-SAPO-34 is illustrated in ***Figure 32*** **c**. The same arguments for the lack of long-range order in SAPO-34 discussed in above, also applies in this case. The fact that the same amorphous morphology was also obtained in this step-up, further strengthens the case for this lack of long range order in some parts of the SAPO-34 structure.

Also, the homogenous distribution of strain visualised in the reconstructions for the Si wafer case is also seen in the capillary set-up.

### 5.7.3. JM-Cu/SAPO-34 in a capillary under humid conditions

Since it has been established that the strain throughout the reconstructed object is homogenous at room temperature and room conditions, the next step was to evaluate the effects of high temperature and humid conditions on the obtained strain contours. For this experiment only JM-Cu/SAPO-34 was analysed. As described in ***Chapter III***, the water bath used to produce the water vapour to be flown throughout the capillary was first ramped to a temperature of 50 $^{o}$C and allowed to decrease to room temperature. It was assumed that a decrease in the temperature of the water bath would lead to an overall reduction of the humidity levels within the capillary. The reconstructions from the phase retrieval algorithm, illustrated in ***Figure 33***, show that the initial reconstruction shows a greater number of phase domains than for the other (where temperature and thus humidity will be much lower). The fact that the phase, and thus the strain, contour goes back to a more homogenous distribution of the phase may mean the mechanism via which the strain is generated is *reversible*. However, this challenges the findings made by Leistner *et al*.,[7] as they stated that, in the case of the Cu sites re-arranging themselves into an inactive catalytic form and this process was no *reversible* form.

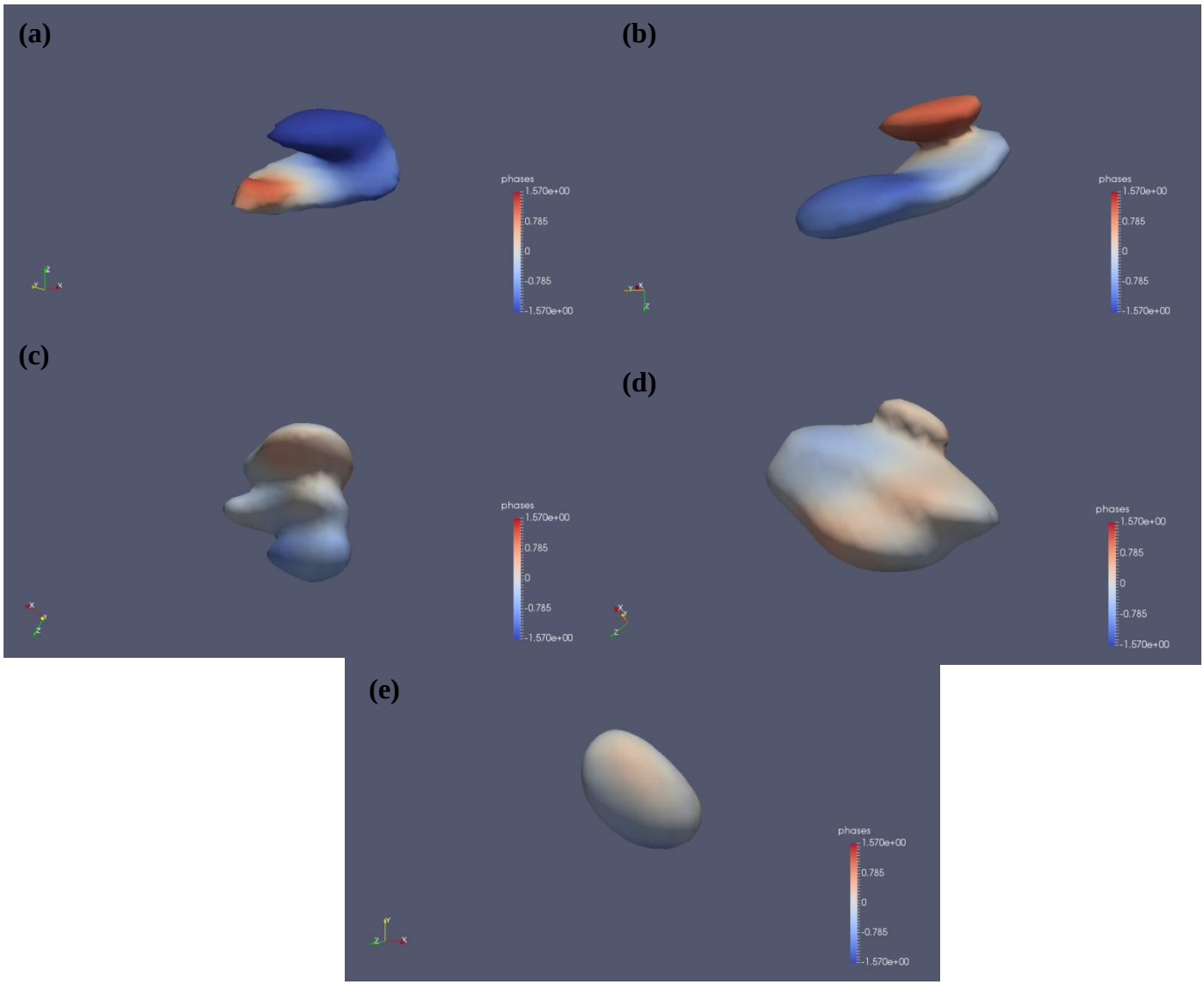


***Figure 33.*** The three dimensional reconstruction of the JM-Cu/SAPO-34. From ***(a) - (e)*** the humidity inside capillary decreases, as well as the temperature of the water bath.

# Future Work

Following the results and discussions made throughout this document, it is clear that a significant amount of work still needs to be performed in order to obtain a clear idea with regards to mechanisms that lead to the low hydrothermal stability in Cu/SAPO-34. To do so a number of future steps have been proposed and these are enumerated in this chapter.

**Computational**

It is clear that the results yielded thus far point towards the possibility of NTE behaviour not only in SAPO-34, independently of which extra-framework ion used; albeit there is some small differences as the extent of contraction between H/SAPO-34 and Cu/SAPO-34. The next logical step is to attempt to produce results for these models in the presence of $H_2O$ molecules. If the lattice dynamics approach continues to be problematic, one could attempt and use molecular dynamics instead; which are likely to be more computationally expensive. The molecular modelling results yielded for Cu/SAPO-34 were done for configuration wherein the extra-framework ion is present at an 8MR. As seen in ***Chapter II,*** the Cu ion may be is also likely found in 6 MR. Thus a more thorough study to evaluate if the NTE prediction still holds true independent on the MR should be performed. Another interesting investigation to perform would be the evaluation of $NO_x$ diffusion rates and the effect of the NTE behaviour in them. This would probably have to be performed via DFT or via some QM/MM methodology because no potentials for the interactions between $NO_x$ and a zeolites network have been found.

**Experimental**

**PXRD**

The results of the PXRD experiment shown in this investigation were only done for two data points of temperature. In order to strengthen the argument for the possession of NTE behaviour in SAPO-34, and thus backing up the theoretical predictions elucidated by the modelling portion of the work, more data points should be taken. Alas, it would also be useful to perform the same experiment not only on Cu/SAPO-34, as it was done here, but also on SAPO-34 frameworks with different extra-framework ions; this would enable one to

determine whether the NTE behaviour is independent of the extra-framework ion; again, as proposed by the theoretical predictions.

**BCDI**

Some work still needs to be done with regards to the application of BCDI in this problem. Firstly, a more sophisticated set-up for the capillary experiment should be developed; one that perhaps could keep track of temperature, humidity etc. Secondly, in addition to the water vapour, $NO_x$ gas in should be attempted as flowing gas in this experiment; and later perhaps having some gas mix that contained air and $NO_x$. Thirdly, ensure that the algorithms used for the reconstruction of the crystals are competent enough to achieve the right solution.

# Conclusions

A lot interest has been paid in the use of Cu/SAPO-34 for $NH_3$-SCR, the reduction of $NO_x$ in the present of ammonia. However, there have reports that, in spite of being very good at converting NO*x* into $N_2$ and $H_2O$, less hazardous gases to the atmosphere, Cu/SAPO-34 has poor hydrothermal stability at relatively low temperature. One of the arguments is that this catalytic deactivation is achieved as a result of a re-arrangement of the Cu sites in the zeolite into an inactive form.

In the light of this information, this study aimed to find out what effect the presence of water has on structure distorting phenomena, such as NTE or the development of strain in the crystal structure in the present of water. The former case aimed to be tackled via molecular modelling methodologies, whereas the latter using an imaging technique called BCDI.

In the case of the molecular modelling work, it was concluded that AlPO-34, H/SAPO-34 and Cu/SAPO-34 all display NTE behaviour, that takes place via the RUMs mechanism. It was also concluded that an increased concentration of Si appears to damp the NTE behaviour, since the values of αl and $\alpha_V$ become more steadily positive as a function of the Si concentration.

From the experimental work, a PXRD investigation on Cu/SAPO-34 successfully predicted NTE behaviour as well. However, the values of the lattice parameters were not equal to those predicted via the modelling work. It was proposed that most probable reason was either the lack of electronic effects being incorporated into the calculations; which may place some role. Or, more realistically, the fact that the models used may be very different with regards the existing Si and Cu relative distributions in the structure. Finally, the results of the BCDI experiment revealed that high humidity levels increase the number of phase the domains in the contour produced by the method. Since there is a relationship of proportionality between the change in phase and the strain, this means that the Cu/SAPO-34 crystals were more structurally strained than when in less humid conditions.

Overall, this work gave some insight and positive results in a number of ways. Taking into account that this was just the very beginning of the project there is no doubt that great results will be coming out of the pipeline in months or years to come.

# References


1 M. Meinshausen, N. Meinshausen, W. Hare, S. C. B. Raper, K. Frieler, R. Knutti, D. J. Frame and M. R. Allen, *Nature*, 2009, **458**, 1158–1162.

2

3 C. T. Bowman, *Symp. Combust.*, 1992, **24**, 859–878.

4

5 B. Smit and T. L. M. Maesen, *Nature*, 2008, **451**, 671–678.

6 2015.

7 K. Leistner and L. Olsson, *Appl. Catal. B Environ.*, 2015, **165**, 192–199.

8 G. D. Barrera and et al., *J. Phys. Condens. Matter*, 2005, **17**, R217.

9 G. Xiong, O. Moutanabbir, M. Reiche, R. Harder and I. Robinson, *Adv. Mater.*, 2014, **26**, 7747–7763.

10

11 J. Weitkamp, *Solid State Ionics*, 2000, **131**, 175–188.

12 M. E. Davis, *ChemInform*, 2002, **33**, 245.

13 J. A. Martens, C. Janssens, P. J. Grobet, H. K. Beyer and P. A. Jacobs, 1989, pp. 215–225.

14 D. Barthomeuf, *J. Phys. Chem.*, 1993, **97**, 10092–10096.

15 G. Sastre, D. W. Lewis and C. R. A. Catlow, *J. Phys. Chem.*, 1996, **100**, 6722–6730.

16 J. Xue, X. Wang, G. Qi, J. Wang, M. Shen and W. Li, *J. Catal.*, 2013, **297**, 56–64.

17 B. Arstad, A. Lind, J. H. Cavka, K. Thorshaug, D. Akporiaye, D. Wragg, H. Fjellvåg, A. Grønvold and T. Fuglerud, *Microporous Mesoporous Mater.*, 2016, **225**, 421–431.

18 R. Martínez-Franco, M. Moliner, C. Franch, A. Kustov and A. Corma, *Appl. Catal. B Environ.*, 2012, **127**, 273–280.

19 Y. Iwase, K. Motokura, T. Koyama, A. Miyaji and T. Baba, *Phys. Chem. Chem. Phys.*, 2009, **11**, 9268.

20 W. A. Sławiński, D. S. Wragg, D. Akporiaye and H. Fjellvåg, *Microporous Mesoporous Mater.*, 2014, **195**, 311–318.

21

22 S. Faizi and C. Fisher, *Chem Wiki*.

23 Wired, .

24 J. S. O. Evans, T. A. Mary and A. W. Sleight, *J. Solid State Chem.*, 1998, **137**, 148–160.

25 J. S. O. Evans, W. I. F. David and A. W. Sleight, *Acta Crystallogr. Sect. B Struct. Sci.*, 1999, **55**, 333–340.

26 S. Sen, R. R. Wusirika and R. E. Youngman, *Microporous Mesoporous Mater.*, 2006, **87**, 217–223.

27 W. Cha, N. C. Jeong, S. Song, H. Park, T. C. Thanh Pham, R. Harder, B. Lim, G. Xiong, D. Ahn, I. McNulty, J. Kim, K. B. Yoon, I. K. Robinson and H. Kim, *Nat. Mater.*, 2013, **12**, 729–34.

28 P. Lightfoot, D. A. Woodcock, M. J. Maple, L. A. Villaescusa and P. A. Wright, *J. Mater. Chem.*, 2001, **11**, 212–216.

29 M. P. Attfield and A. W. Sleight, *Chem. Mater.*, 1998, **10**, 2013–2019.

30 D. Dubbeldam, K. S. Walton, D. E. Ellis and R. Q. Snurr, *Angew. Chemie Int. Ed.*, 2007, **46**, 4496–4499.

31 A. L. Goodwin, M. Calleja, M. J. Conterio, M. T. Dove, J. S. O. Evans, D. A. Keen, L. Peters and M. G. Tucker, *Science (80-. ).*, 2008, **319**, 794–797.

32 A. W. Sleight, *Endeavour*, 1995, **19**, 64–68.
33 A. W. Sleight, *Curr. Opin. Solid State Mater. Sci.*, 1998, **3**, 128–131.
34 A. P. Ramirez, G. Ernst, C. Broholm and G. R. Kowach, *Nature*, 1998, **396**, 147–149.
35 I. D. Brown and R. D. Shannon, *Acta Crystallogr. Sect. A*, 1973, **29**, 266–282.
36 M. T. Dove, *Am. Mineral.*, 1997, **82**, 213–244.
37 C. D. Chandler, C. Roger and M. J. Hampden-Smith, *Chem. Rev.*, 1993, **93**, 1205–1241.
38 A. Bieniok and K. D. Hammonds, *Microporous Mesoporous Mater.*, 1998, **25**, 193–200.
39 P. Tschaufeser and S. C. Parker, *J. Phys. Chem*, 1995, **99**, 10609–10615.
40 B. A. Marinkovic, P. M. Jardim, A. Saavedra, L. Y. Lau, C. Baehtz, R. R. de Avillez and F. Rizzo, *Microporous Mesoporous Mater.*, 2004, **71**, 117–124.
41 K. D. Hammonds, M. T. Dove, A. P. Giddy, V. Heine and B. Winkler, *Am. Mineral.*, 1996, **81**, 1057–1079.
42 J. . Tao and A. . Sleight, *J. Solid State Chem.*, 2003, **173**, 442–448.
43 W. Miller, C. W. Smith, D. S. MacKenzie and K. E. Evans, *J. Mater. Sci.*, 2009, **44**, 5441–5451.
44 A. K. A. Pryde, K. D. Hammonds, M. T. Dove, V. Heine, J. D. Gale and M. C. Warren, *J. Phys. Condens. Matter*, 1996, **8**, 10973–10982.
45 J. Arvanitidis, K. Papagelis, S. Margadonna, K. Prassides and A. N. Fitch, *Nature*, 2003, **425**, 599–602.
46 R. D. Shannon, *Acta Crystallogr. Sect. A*, 1976, **32**, 751–767.
47 I. Yamada, K. Tsuchida, K. Ohgushi, N. Hayashi, J. Kim, N. Tsuji, R. Takahashi, M. Matsushita, N. Nishiyama, T. Inoue, T. Irifune, K. Kato, M. Takata and M. Takano, *Angew. Chemie Int. Ed.*, 2011, **50**, 6579–6582.
48 Y. W. Long, N. Hayashi, T. Saito, M. Azuma, S. Muranaka and Y. Shimakawa, *Nature*, 2009, **458**, 60–3.
49 Y. Long and Y. Shimakawa, *New J. Phys.*, 2010, **12**.
50 M. Azuma, W. Chen, H. Seki, M. Czapski, S. Olga, K. Oka, M. Mizumaki, T. Watanuki, N. Ishimatsu, N. Kawamura, S. Ishiwata, M. G. Tucker, Y. Shimakawa and J. P. Attfield, *Nat. Commun.*, 2011, **2**, 347.
51 G. C. E, *C.R. Acad. Sci.*, 1897, **125**, 235.
52 J. C. Lin, P. Tong, W. Tong, S. Lin, B. S. Wang, W. H. Song, Y. M. Zou and Y. P. Sun, *Appl. Phys. Lett.*, 2015, **106**, 1–16.
53 T. Varga, J. L. Moats, S. V. Ushakov and A. Navrotsky, *J. Mater. Res.*, 2007, **22**, 2512–2521.
54 J. S. . Evans and T. . Mary, *Int. J. Inorg. Mater.*, 2000, **2**, 143–151.
55 M. Ardit, A. Martucci and G. Cruciani, *J. Phys. Chem. C*, 2015, **119**, 7351–7359.
56 G. Cruciani, *J. Phys. Chem. Solids*, 2006, **67**, 1973–1994.
57 J. D. Gale, .
58
59 M. T. Dove, *Introduction to Lattice Dynamics*, 1993.
60
61 I. Robinson and R. Harder, *Nat. Mater.*, 2009, **8**, 291–298.
62 W. Miller, D. S. Mackenzie, C. W. Smith and K. E. Evans, *Mech. Mater.*, 2008, **40**, 351–361.
63 M. Ito, Y. Shimoyama, Y. Saito, Y. Tsurita and M. Otake, *Acta Crystallogr. Sect. C Cryst. Struct. Commun.*, 1985, **41**, 1698–1700.
64 G. Sastre, D. W. Lewis, C. Richard and A. Catlow, *J. Phys. Chem. B*, 1997, **101**, 5249–5262.

# Appendix

*Appendix 1: Tabulated values of static lattice geometry optimisation of H/SAPO-34*

| | O1 | | | | | | | | |
|---|---|---|---|---|---|---|---|---|---|
| **Si molar ratio / %** | ***a / Å*** | ***b / Å*** | ***c / Å*** | **α / °** | **β / °** | **γ / °** | **Volume / Å$^3$** | **Energy per Al / eV** | **Gnorm / eV Å$^{-1}$** |
| 0 | 9.291 | 9.291 | 9.291 | 94.9 | 94.9 | 94.9 | 704 | -267.979 | 3.5E-05 |
| 2.1 | 9.295 | 9.298 | 9.298 | 94.9 | 94.9 | 94.9 | 706 | -266.751 | 3.4E-05 |
| 4.2 | 9.302 | 9.302 | 9.306 | 94.8 | 94.9 | 94.8 | 708 | -265.522 | 3.9E-06 |
| 6.3 | 9.307 | 9.311 | 9.313 | 94.8 | 94.8 | 94.7 | 709 | -264.294 | 4.9E-06 |
| 8.4 | 9.310 | 9.319 | 9.321 | 94.7 | 94.8 | 94.6 | 711 | -263.066 | 8.4E-06 |
| | **O2** | | | | | | | | |
| **Si molar ratio / %** | ***a / Å*** | ***b / Å*** | ***c / Å*** | **α / °** | **β / °** | **γ / °** | **Volume / Å$^3$** | **Energy per Al / eV** | **Gnorm / eV Å$^{-1}$** |
| 0 | 9.291 | 9.291 | 9.291 | 95.0 | 94.9 | 94.9 | 704 | -267.979 | 3.5E-05 |
| 2.1 | 9.298 | 9.292 | 9.300 | 94.9 | 94.9 | 94.9 | 705 | -266.748 | 4.00E-08 |
| 4.2 | 9.308 | 9.300 | 9.288 | 94.9 | 94.8 | 94.9 | 706 | -265.509 | 1.03E-05 |
| 6.3 | 9.306 | 9.307 | 9.312 | 94.9 | 94.9 | 95.0 | 708 | -264.295 | 7.89E-06 |
| 8.4 | 9.310 | 9.314 | 9.320 | 94.9 | 95.0 | 95.0 | 709 | -263.068 | 8.88E-06 |
| | **O3** | | | | | | | | |
| **Si molar ratio / %** | ***a / Å*** | ***b / Å*** | ***c / Å*** | **α / °** | **β / °** | **γ / °** | **Volume / Å$^3$** | **Energy per Al / eV** | **Gnorm / eV Å$^{-1}$** |
| 0 | 9.291 | 9.291 | 9.291 | 95.0 | 95.0 | 95.0 | 704 | -267.979 | 3.5E-05 |
| 2.1 | 9.294 | 9.297 | 9.298 | 95.0 | 95.0 | 95.0 | 705 | -266.751 | 1.03E-05 |
| 4.2 | 9.302 | 9.300 | 9.305 | 95.0 | 95.0 | 95.0 | 707 | -265.523 | 8.88E-06 |
| 6.3 | 9.306 | 9.307 | 9.312 | 95.0 | 95.0 | 95.0 | 708 | -264.295 | 7.89E-06 |
| 8.4 | 9.310 | 9.314 | 9.320 | 95.0 | 95.0 | 95.0 | 710 | -263.068 | 8.88E-06 |
| | **O4** | | | | | | | | |
| **Si molar ratio / %** | ***a / Å*** | ***b / Å*** | ***c / Å*** | **α / °** | **β / °** | **γ / °** | **Volume / Å$^3$** | **Energy per Al / eV** | **Gnorm / eV Å$^{-1}$** |
| 0 | 9.291 | 9.291 | 9.291 | 95.0 | 95.0 | 95.0 | 704 | -267.979 | 3.5E-05 |
| 2.1 | 9.293 | 9.295 | 9.300 | 95.0 | 95.0 | 95.0 | 705 | -266.748 | 6.35E-06 |
| 4.2 | 9.303 | 9.296 | 9.304 | 95.0 | 95.1 | 95.0 | 707 | -265.516 | 1.08E-05 |
| 6.3 | 9.304 | 9.302 | 9.313 | 95.1 | 95.1 | 95.0 | 708 | -264.284 | 2.81E-05 |
| 8.4 | 9.306 | 9.306 | 9.323 | 95.2 | 95.1 | 95.0 | 709 | -263.051 | 6.90E-06 |

*Appendix 2: The 'corrected' lattice parameters and unit cell volume of H/SAPO-34.*

| | O1 | | |
|---|---|---|---|
| **Si molar ratio / %** | **a** | **alpha** | **unit cell volume** |
| 0 | 9.291 | 94.9 | 783 |
| 2.1 | 9.297 | 94.9 | 785 |
| 4.2 | 9.304 | 94.8 | 787 |
| 6.3 | 9.310 | 94.8 | 789 |
| 8.4 | 9.317 | 94.7 | 791 |
| | **O2** | | |
| **Si molar ratio / %** | **a** | **alpha** | **unit cell volume** |
| 0 | 9.291 | 94.9 | 783 |
| 2.1 | 9.297 | 94.9 | 785 |
| 4.2 | 9.299 | 94.9 | 786 |
| 6.3 | 9.308 | 95.0 | 787 |
| 8.4 | 9.315 | 95.0 | 789 |
| | **O3** | | |
| **Si molar ratio / %** | **a** | **alpha** | **unit cell volume** |
| 0 | 9.291 | 94.9 | 783 |
| 2.1 | 9.296 | 95.0 | 784 |
| 4.2 | 9.302 | 95.0 | 786 |
| 6.3 | 9.308 | 95.0 | 787 |
| 8.4 | 9.315 | 95.0 | 789 |
| | **O4** | | |
| **Si molar ratio / %** | **a** | **alpha** | **unit cell volume** |
| 0 | 9.291 | 94.9 | 783 |
| 2.1 | 9.296 | 95.0 | 784 |
| 4.2 | 9.301 | 95.0 | 785 |
| 6.3 | 9.306 | 95.0 | 786 |
| 8.4 | 9.312 | 95.1 | 787 |

***Appendix 3: The 'corrected' lattice parameters and unit cell volume of AlPO-34 for the NTE prediction.***

| Temperature / K | *A* / *Å* | α / ° | Volume / Å$^3$ |
|---|---|---|---|
| 0 | 9.299 | 94.9 | 795 |
| 100 | 9.295 | 94.9 | 794 |
| 200 | 9.287 | 94.9 | 792 |
| 300 | 9.279 | 94.9 | 790 |
| 400 | 9.271 | 94.9 | 788 |
| 500 | 9.263 | 94.9 | 785 |

*Appendix 4: The 'corrected' lattice parameters and unit cell volume of H/SAPO-34 for the NTE prediction. (O1 only)*

| | 2.1 % Si | | |
|---|---|---|---|
| **Temperature / K** | ***A / Å*** | **α / °** | **Unit cell Volume / Å$^3$** |
| 0 | 9.302 | 94.9 | 786 |
| 100 | 9.298 | 94.9 | 785 |
| 200 | 9.291 | 94.9 | 783 |
| 300 | 9.282 | 94.9 | 781 |
| 400 | 9.274 | 94.9 | 779 |
| 500 | 9.266 | 94.9 | 777 |
| | **4.2 % Si** | | |
| **Temperature / K** | ***A / Å*** | **α / °** | **Unit cell Volume / Å$^3$** |
| 0 | 9.306 | 94.9 | 787 |
| 100 | 9.302 | 94.9 | 786 |
| 200 | 9.294 | 94.9 | 784 |
| 300 | 9.286 | 94.9 | 782 |
| 400 | 9.277 | 94.9 | 780 |
| 500 | 9.269 | 94.9 | 778 |
| | **6.3 % Si** | | |
| **Temperature / K** | ***A / Å*** | **α / °** | **Unit cell Volume / Å$^3$** |
| 0 | 9.301 | 94.9 | 786 |
| 100 | 9.298 | 94.9 | 785 |
| 200 | 9.293 | 94.9 | 784 |
| 300 | 9.288 | 94.9 | 783 |
| 400 | 9.282 | 94.9 | 781 |
| 500 | 9.277 | 94.9 | 780 |
| | **8.4 % Si** | | |
| **Temperature / K** | ***A / Å*** | **α / °** | **Unit cell Volume / Å$^3$** |
| 0 | 9.312 | 94.9 | 789 |
| 100 | 9.308 | 94.9 | 788 |
| 200 | 9.300 | 94.9 | 786 |
| 300 | 9.292 | 94.9 | 783 |
| 400 | 9.284 | 94.9 | 781 |
| 500 | 9.275 | 94.9 | 779 |

***Appendix 5: The 'corrected' lattice parameters and unit cell volume of Cu/SAPO-34 (mixed) for the NTE prediction.***

| | 6.3 % Si | | |
|---|---|---|---|
| **Temperature / K** | ***A / Å*** | **α / °** | **Unit cell Volume / Å$^3$** |
| 0 | 9.304 | 95.3 | 783 |
| 100 | 9.301 | 95.3 | 783 |
| 200 | 9.294 | 95.3 | 781 |
| 300 | 9.287 | 95.2 | 780 |
| 400 | 9.279 | 95.2 | 778 |
| 500 | 9.272 | 95.2 | 776 |

| | 8.4 % Si | | |
|---|---|---|---|
| **Temperature / K** | ***A / Å*** | **α / °** | **Unit cell Volume / Å$^3$** |
| 0 | 9.305 | 95.5 | 782 |
| 100 | 9.301 | 95.5 | 781 |
| 200 | 9.294 | 95.5 | 779 |
| 300 | 9.286 | 95.5 | 777 |
| 400 | 9.279 | 95.5 | 776 |
| 500 | 9.271 | 95.5 | 774 |

*Appendix 5: The 'corrected' lattice parameters and unit cell volume of $Cu^{+}$/SAPO-34 for the NTE prediction.*

| | 2.1 % Si | | |
|---|---|---|---|
| **Temperature / K** | ***A* / Å** | **α / °** | **Unit cell Volume / Å$^3$** |
| 0 | 9.302 | 94.9 | 786 |
| 100 | 9.298 | 94.9 | 785 |
| 200 | 9.291 | 94.9 | 783 |
| 300 | 9.282 | 94.9 | 781 |
| 400 | 9.274 | 94.9 | 779 |
| 500 | 9.266 | 94.9 | 777 |
| | **4.2 % Si** | | |
| **Temperature / K** | ***A* / Å** | **α / °** | **Unit cell Volume / Å$^3$** |
| 0 | 9.306 | 94.9 | 787 |
| 100 | 9.302 | 94.9 | 786 |
| 200 | 9.294 | 94.9 | 784 |
| 300 | 9.286 | 94.9 | 782 |
| 400 | 9.277 | 94.9 | 780 |
| 500 | 9.269 | 94.9 | 778 |
| | **6.3 % Si** | | |
| **Temperature / K** | ***A* / Å** | **α / °** | **Unit cell Volume / Å$^3$** |
| 0 | 9.301 | 94.9 | 786 |
| 100 | 9.298 | 94.9 | 785 |
| 200 | 9.293 | 94.9 | 784 |
| 300 | 9.288 | 94.9 | 783 |
| 400 | 9.282 | 94.9 | 781 |
| 500 | 9.277 | 94.9 | 780 |
| | **8.4 % Si** | | |
| **Temperature / K** | ***A* / Å** | **α / °** | **Unit cell Volume / Å$^3$** |
| 0 | 9.312 | 94.9 | 789 |
| 100 | 9.308 | 94.9 | 788 |
| 200 | 9.300 | 94.9 | 786 |
| 300 | 9.292 | 94.9 | 783 |
| 400 | 9.284 | 94.9 | 781 |
| 500 | 9.275 | 94.9 | 779 |